

## OBSERVATIONS OF T TAURI DISKS AT SUB-AU RADII: IMPLICATIONS FOR MAGNETOSPHERIC ACCRETION AND PLANET FORMATION

J. A. EISNER,<sup>1</sup> L. A. HILLENBRAND,<sup>1</sup> R. J. WHITE,<sup>1</sup> R. L. AKESON,<sup>2</sup> AND A. I. SARGENT<sup>1</sup>

*Received 2004 October 15; accepted 2005 January 12*

### ABSTRACT

We determine inner disk sizes and temperatures for four solar-type ( $1\text{--}2 M_{\odot}$ ) classical T Tauri stars, AS 207A, V2508 Oph, AS 205A, and PX Vul, using  $2.2 \mu\text{m}$  observations from the Keck Interferometer. Nearly contemporaneous near-IR adaptive optics imaging photometry, optical photometry, and high-dispersion optical spectroscopy are used to distinguish contributions from the inner disks and central stars in the interferometric observations. In addition, the spectroscopic and photometric data provide estimates of stellar properties, mass accretion rates, and disk corotation radii. We model our interferometric and photometric data in the context of geometrically flat accretion disk models with inner holes, and flared disks with puffed-up inner walls. Models incorporating puffed-up inner disk walls generally provide better fits to the data, similar to previous results for higher mass Herbig Ae stars. Our measured inner disk sizes are larger than disk truncation radii predicted by magnetospheric accretion models, with larger discrepancies for sources with higher mass accretion rates. We suggest that our measured sizes correspond to dust sublimation radii, and that optically thin gaseous material may extend farther inward to the magnetospheric truncation radii. Finally, our inner disk measurements constrain the location of terrestrial planet formation as well as potential mechanisms for halting giant planet migration.

*Subject headings:* circumstellar matter — stars: individual (AS 205, AS 207, PX Vulpeculae, V2508 Ophiuchi) — stars: pre-main-sequence — techniques: high angular resolution — techniques: interferometric

### 1. INTRODUCTION

T Tauri stars are low-mass ( $\lesssim 2 M_{\odot}$ ) pre-main-sequence objects, thought to be early analogs of stars like our own Sun. A wealth of evidence, including direct imaging at millimeter and optical wavelengths (e.g., Koerner & Sargent 1995; Dutrey et al. 1996; McCaughrean & O’Dell 1996) and modeling of spectral energy distributions (SEDs; e.g., Adams et al. 1988; Bertout et al. 1988; Beckwith et al. 1990), has confirmed the long-espoused hypothesis that T Tauri stars are surrounded by massive disks of dust and gas. Moreover, observed line profiles and UV continuum excesses indicate that T Tauri stars are actively accreting material from their circumstellar disks (e.g., Walker 1972; Edwards et al. 1994; Gullbring et al. 1998).

The structure of the innermost disk regions may reveal the mechanism by which material is accreted through the disk onto the star. In the current paradigm, T Tauri disks are truncated by the stellar magnetosphere within the corotation radius, with material accreting along magnetic field lines onto high-latitude regions of the star (e.g., Königl 1991; Shu et al. 1994). For typical T Tauri star masses, radii, magnetic field strengths, and accretion rates, predicted truncation radii range from  $\sim 0.02$  to  $0.2$  AU. Observational measurements of these truncation radii are an obviously important test of the theory of magnetospheric accretion.

The spatial and temperature structures of inner circumstellar disks are also important for understanding the properties of dust and gas in the terrestrial planet region, and ultimately for understanding the formation of planets. For example, a puffed-up inner disk wall, because of the normal angle of incidence of stellar radiation on the truncated inner edge (e.g., Dullemond et al. 2001), may lead to shadowing and thus cooler temper-

atures in the inner disk compared to standard flat or flared disk temperature profiles (e.g., Chiang & Goldreich 1997). This, in turn, would have profound implications as to how and where terrestrial planets form (e.g., Hayashi 1981; Sasselov & Lecar 2000). Furthermore, inner disk structure is important for understanding how the close-in extrasolar planets discovered by radial velocity surveys (e.g., Marcy & Butler 2000) either formed at, or migrated to, their observed orbital radii (e.g., Lin et al. 1996).

Currently, only near-IR interferometric observations have sufficient spatial resolution to probe directly the geometry and temperature of hot ( $\sim 1000\text{--}2000$  K) disk regions within  $\sim 1$  AU of young stars. Observations of the inner disks of a few of the brightest T Tauri stars (Akeson et al. 2000; Colavita et al. 2003) and of their more massive counterparts, Herbig Ae stars (Millan-Gabet et al. 1999, 2001; Eisner et al. 2003, 2004), demonstrated that inner disks around lower mass stars ( $\lesssim 5 M_{\odot}$ ) are larger than inferred by fitting geometrically thin accretion disk models to SEDs (e.g., Beckwith et al. 1990). Inclusion of puffed-up inner walls in the models leads to consistent fits to both interferometric and SED data for these objects (Eisner et al. 2004; Muzerolle et al. 2003). On the other hand, higher mass Herbig Be stars (Eisner et al. 2004) and the extreme accretor FU Ori (Malbet et al. 1998, 2005) are fitted well with simple flat disk models, suggesting that inner disk structure may depend on accretion rates or stellar properties. A larger sample of resolved inner disks, including lower mass T Tauri stars, is necessary to explore such trends.

Here, we present  $2.2 \mu\text{m}$  Keck Interferometer (KI) observations of the inner disks around four solar-type ( $1\text{--}2 M_{\odot}$ ) T Tauri stars, potential analogs to our own young Sun. In order to model the stellar and circumstellar emission accurately, we combine our spatially resolved interferometry data with optical/near-IR SEDs and high-resolution echelle spectra. The photometric and spectroscopic data are essential for decomposition of the observed  $2.2 \mu\text{m}$  flux into stellar and excess components.

<sup>1</sup> Department of Astronomy, California Institute of Technology, MC 105-24, Pasadena, CA 91125; jae@astro.caltech.edu.

<sup>2</sup> Michelson Science Center, California Institute of Technology, MC 100-22, Pasadena, CA 91125.

TABLE 1  
OBSERVED PROPERTIES OF SAMPLE

| SOURCE          | $\alpha$<br>(J2000.0) | $\delta$<br>(J2000.0) | $d$<br>(pc)      | SPECTRAL<br>TYPE          | $r_R$           | $r_I$            | $v \sin i$<br>(km s <sup>-1</sup> ) | $v_{\text{helio}}$<br>(km s <sup>-1</sup> ) | H $\alpha$ |              |
|-----------------|-----------------------|-----------------------|------------------|---------------------------|-----------------|------------------|-------------------------------------|---|------------|--------------|
|                 |                       |                       |                  |                           |                 |                  |                                     |   | EW         | 10%<br>width |
| AS 207A .....   | 16 27 40.28           | -24 22 04.0           | 160 <sup>a</sup> | K5 $\pm$ 1                | 0.04 $\pm$ 0.07 | -0.07 $\pm$ 0.15 | 15.2 $\pm$ 0.9                      | -7.17 $\pm$ 0.25                            | -16.4      | 342          |
| V2508 Oph ..... | 16 48 45.62           | -14 16 35.9           | 160 <sup>a</sup> | K6 $\pm$ 1                | 0.27 $\pm$ 0.07 | 0.09 $\pm$ 0.10  | 22.9 $\pm$ 1.0                      | -8.26 $\pm$ 0.56                            | -32.5      | 278          |
| AS 205A .....   | 16 11 31.40           | -18 38 24.5           | 160 <sup>a</sup> | K5 $\pm$ 1                | 2.94 $\pm$ 0.32 | 1.95 $\pm$ 0.20  | 14.9 $\pm$ 1.8                      | -11.60 $\pm$ 0.87                           | -99.6      | 388          |
| PX Vul .....    | 19 26 40.30           | +23 53 49.0           | 420 <sup>b</sup> | F3 $\pm$ 2 <sup>c,d</sup> | 0.82 $\pm$ 0.39 | 0.62 $\pm$ 0.45  | 78 $\pm$ 11                         | -7.0 $\pm$ 2.5                              | -9.4       | 512          |

NOTES.—Units of right ascension are hours, minutes, and seconds, and units of declination are degrees, arcminutes, and arcseconds. Spectral types, veilings (ratios of excess to stellar flux) at  $R$  and  $I$  bands,  $v \sin i$  values, heliocentric radial velocities, H $\alpha$  EWs, and H $\alpha$  widths at 10% of the peak are determined from high-resolution optical spectroscopy (§ 2.5). Distance estimates are likely uncertain by 10%–20%.

<sup>a</sup> Chini (1981).

<sup>b</sup> Herbst et al. (1982).

<sup>c</sup> Mora et al. (2001).

<sup>d</sup> Hernández et al. (2004).

Since T Tauri stars are variable at near-IR wavelengths on time-scales of several days to months (e.g., Skrutskie et al. 1996), our spectroscopic, photometric, and interferometric data were obtained within several days of one another. The photometry and spectra also enable determination of various properties of these systems, including stellar masses, ages, temperatures, radii,  $v \sin i$ , binarity, mass accretion rates, magnetospheric truncation radii, and corotation radii.

From the 2.2  $\mu\text{m}$  interferometry data, we establish inner disk radii and temperatures, and distinguish between flat and puffed-up inner disk models. In addition, we compare these measured sizes with inferred magnetospheric and corotation radii. Although our sample is small, the range of stellar and accretion properties allows us to explore how inner disk structure depends on these parameters.

## 2. OBSERVATIONS AND DATA REDUCTION

### 2.1. Sample

Our sample consists of four classical T Tauri stars: AS 207A, V2508 Oph, AS 205A, and PX Vul. AS 207A, the optically brightest T Tauri star in  $\rho$  Oph, was identified as a young star based on its H $\alpha$  emission (Struve & Rudkjøbing 1949) and also as one component of a 0<sup>h</sup>.6 binary system (Ghez et al. 1993). The T Tauri star V2508 Oph (Walter 1986) is located near the L162 dark cloud. AS 205A is a well-known young star near the  $\nu$  Sco dark nebula (e.g., Merrill & Burwell 1950), identified as the brightest component of a 1<sup>h</sup>.3 binary system by Ghez et al. (1993). We assume that AS 207A, V2508 Oph, and AS 205A are all at the approximate distance of the  $\rho$  Oph cloud, 160 pc (Chini 1981). Finally, PX Vul is a T Tauri star in the Vul R2 region, at a distance of 420 pc (e.g., Herbig & Kameswara Rao 1972; Herbst et al. 1982). Properties of our sample, including celestial coordinates, distances, and spectral types, are included in Table 1.

### 2.2. 2.2 $\mu\text{m}$ Interferometry

We observed AS 207A, V2508 Oph, AS 205A, and PX Vul with the KI on 2004 June 2. KI is a fringe-tracking, long baseline, near-IR Michelson interferometer combining light from the two 10 m Keck apertures (Colavita & Wizinowich 2003; Colavita et al. 2003). The fringe tracker detects a source in a 5 ms integration, setting a limiting  $K$ -band magnitude of  $m_K \sim 9$ . In addition, sources must be optically bright enough for the adaptive optics (AO) systems on each Keck aperture. Superb seeing ( $\lesssim 0\prime.5$ ) allowed excellent AO performance for our sample.

For each target, we measured squared visibilities ( $V^2$ ) at  $K$  band ( $\lambda_0 = 2.2 \mu\text{m}$ ,  $\Delta\lambda = 0.4 \mu\text{m}$ ). The system visibility (i.e., the point-source response of the interferometer), was measured using observations of unresolved calibrators, weighted by the internal scatter in the calibrator and the temporal and angular proximity to the target source (Boden et al. 1998). Source and calibrator data were corrected for detection biases as described by Colavita (1999) and averaged into 5 s blocks. The calibrated  $V^2$  for the target sources are the average of the 5 s blocks in each integration, with uncertainties given by the quadrature addition of the internal scatter and the uncertainty in the system visibility. Typical uncertainties are  $\sim 5\%$ .

All calibrators were chosen to be compact (angular diameters  $\lesssim 0.2$  mas) and close to the target sources (within  $\sim 10^\circ$ ). In addition, our calibrators have  $K$ -band magnitudes similar to those of our targets, to minimize potential biases. At optical wavelengths, the calibrators are brighter than the targets, which may lead to enhanced AO performance; by measuring the photon counts along both interferometer arms and applying a standard “ratio correction” (e.g., Colavita 1999), we calibrate out the effects of AO performance on the visibilities. The data for AS 207A, V2508 Oph, and AS 205A were calibrated using HD 142943 and HD 148968, and data for PX Vul were calibrated using HD 181383 and HD 182919.

### 2.3. JHK Adaptive Optics Imaging

We obtained dithered imaging observations of our sources at  $J$ ,  $H$ , and  $K$  on 2004 June 4 using the Palomar 200 inch AO system (Troy et al. 2000) with the PHARO camera (Hayward et al. 2001). After bias correction, background subtraction, and flat-fielding of the images, photometric fluxes were measured with respect to the same calibrators used in our KI observations. Calibrator magnitudes are known from the 2MASS catalog, assuming they are nonvariable. The photometric errors are given by the quadrature addition of the rms variations in brightness between source integrations and the uncertainties in the calibrator magnitudes. Since the sources and calibrators were observed at similar air masses, we apply no atmospheric extinction corrections. The measured fluxes for these sources are listed in Table 2.

With the high angular resolution afforded by AO imaging ( $\sim 0\prime.1$  at  $K$  band), we were able to resolve AS 207 and AS 205 into binaries, finding parameters (see Table 3) consistent with previous measurements (Ghez et al. 1993; Reipurth & Zinnecker 1993; Koresko 2002; Barsony et al. 2003). For these systems, we

TABLE 2  
PHOTOMETRY OF OBSERVED SOURCES

| Source                     | <i>U</i>     | <i>B</i>     | <i>V</i>     | <i>R</i>     | <i>I</i>     | <i>J</i>    | <i>H</i>    | <i>K</i>    |
|----------------------------|--------------|--------------|--------------|--------------|--------------|-------------|-------------|-------------|
| AS 207A <sup>a</sup> ..... | 13.52 ± 0.53 | 13.00 ± 0.07 | 11.78 ± 0.09 | 10.95 ± 0.13 | 9.80 ± 0.09  | 8.69 ± 0.05 | 7.96 ± 0.06 | 7.31 ± 0.06 |
| V2508 Oph.....             | 15.74 ± 1.35 | 15.04 ± 0.06 | 13.45 ± 0.03 | 12.29 ± 0.04 | 10.74 ± 0.08 | 8.75 ± 0.04 | 7.73 ± 0.07 | 7.04 ± 0.08 |
| AS 205A <sup>a</sup> ..... | 13.69 ± 0.47 | 13.74 ± 0.06 | 12.76 ± 0.03 | 11.82 ± 0.04 | 10.52 ± 0.08 | 8.63 ± 0.13 | 7.41 ± 0.07 | 6.36 ± 0.08 |
| PX Vul.....                | 12.42 ± 0.38 | 12.35 ± 0.05 | 11.55 ± 0.02 | 11.01 ± 0.09 | 10.32 ± 0.06 | 9.33 ± 0.14 | 8.59 ± 0.09 | 7.74 ± 0.10 |

<sup>a</sup> For AS 207A and AS 205A, which have known companions, the *UBVRI* photometry contains contributions from both components, while the *JHK* photometry reflects only the emission from the primaries.

measured photometric fluxes for both the primaries and secondaries; *JHK* magnitudes for the primaries are listed in Table 2, and  $\Delta JHK$  values are given in Table 3. Since the projected binary separations are much larger than the field of view of KI (50 mas), we obtained interferometric data only for the primaries. No spatially resolved companions brighter than  $\Delta K = 5$  were detected near V2508 Oph or PX Vul, and we consider these to be single stars hereafter.

#### 2.4. *UBVRI* Photometry

We observed our sample through Johnson *U*, *B*, *V*, and Kron *R* and *I* filters on 2004 June 8 using the robotic Palomar 60 inch telescope. Photometric fluxes were measured from bias-corrected, flat-fielded images using well-studied photometric standards (Landolt 1992). We determined extinction corrections and magnitude zero points using observations of five Landolt standards obtained throughout the night. Photometric errors for our target sources are the sum of various uncertainties in quadrature: the rms variation between integrations (where multiple integrations of a source are available), the uncertainties in zero points and extinction coefficients, and uncertainties in magnitudes of our calibrators. Photometric uncertainties are typically  $\lesssim 10\%$ , except at *U* band, where substantial uncertainties in the extinction coefficients lead to large error bars for the measured fluxes.

The seeing-limited resolution of these observations was  $\sim 1''.7$ , and the close binaries in our sample, AS 207 and AS 205, are unresolved. Optical photometry for these sources, listed in Table 2, therefore includes contributions from both the primaries and the secondaries.

#### 2.5. High-Resolution Optical Spectroscopy

High-dispersion optical spectra of the sample were obtained on 2004 June 11 using the HIRES spectrograph (Vogt et al. 1994) on Keck I. HIRES was used with the red collimator, an RG 610 filter, and the D1 decker ( $1''.15 \times 14''.0$ ), yielding  $R \approx 34,000$  spectra over 6330–8750 Å, with gaps between orders. An internal quartz lamp and a ThAr lamp were observed with the same setup for flat-fielding and dispersion correction. Several dwarf spectral type standards with known radial velocities were also observed to assist in the spectroscopic analysis. The binary AS 205 was observed with the slit along the axis of the

pair, while AS 207 (an unresolved binary in these observations), V2508 Oph, and PX Vul were observed with the slit perpendicular to the horizon (vertical mode).

The HIRES spectra were reduced using the facility “MAKEE” reduction script written by Tom Barlow. Reduction includes bias correction, flat-fielding, spectral extraction, sky subtraction, wavelength calibration, and heliocentric radial velocity corrections. This procedure worked well for single stars, but not for the components of AS 205 whose spectra overlap. In that case, the component spectra were determined by fitting two Gaussians to each one-dimensional cut in the spatial direction of the two-dimensional spectra. The FWHMs of the best-fit Gaussians were  $0''.4$ ; the seeing was quite good, and the  $1''.2$  pair is reasonably well resolved. These extracted component spectra were then assigned the wavelength solution of the combined system as determined by MAKEE. Portions of the extracted spectra for our sources are shown in Figure 1.

### 3. ANALYSIS

Calibrated 2.2  $\mu\text{m}$  KI visibilities (§ 2.2) and dereddened SEDs (§§ 2.3–2.4) for our sample are shown in Figures 2–5;  $V^2$  values are plotted as a function of *u-v* radius  $r_{uv}$ , and SEDs use units of  $\lambda F_\lambda$ . The SEDs were constructed from our measured *UBVRIJHK* photometry, corrected for binarity in the case of AS 207 and AS 205 (Table 3; § 3.1.1) and dereddened using the  $A_V$  values in Table 1. Figures 2–5 also include longer wavelength ( $>3 \mu\text{m}$ ) photometry from the literature.

Measured 2.2  $\mu\text{m}$  KI visibilities and broadband SEDs constrain the sizes and temperatures of inner disks around the observed sources. However, the near-IR stellar flux contribution to both the SEDs and visibilities must be removed before modeling the circumstellar component. We determine the stellar properties of our sample in § 3.1.1 based on our spectroscopy and photometry, and use Kurucz models to determine stellar fluxes at near-IR wavelengths (see Figs. 2–5; Table 4). Removing the stellar contributions, we are left with the circumstellar components of the visibilities and SEDs.

We model these circumstellar components in terms of (1) a geometrically flat accretion disk and (2) a flared, two-layer, irradiated disk with a puffed-up inner wall (§ 3.3; as in Eisner et al. 2004). For each source, we compute a grid of models for varying inner disk sizes and temperatures, and find the “best-fit” model for which the  $\chi^2$  between the model and the data is minimized. SEDs and visibilities computed for the best-fit models are shown in Figures 2–5, and best-fit inner disk sizes and temperatures are listed in Table 5. Longer wavelength photometry from the literature is used to qualitatively constrain disk flaring (§ 3.4), although it is not used in our disk model-fitting.

In order to compare our derived inner disk sizes with those expected from magnetospheric accretion theory, we use veiling values and shorter wavelength photometry to constrain mass accretion rates (§ 3.1.2) and thereby determine magnetospheric

TABLE 3  
BINARIES

| Source                     | Separation<br>(arcsec) | P.A.<br>(deg) | $\Delta J$<br>(mag) | $\Delta H$<br>(mag) | $\Delta K$<br>(mag) |
|----------------------------|------------------------|---------------|---------------------|---------------------|---------------------|
| AS 207B.....               | 0.63                   | 354           | 1.59 ± 0.07         | 1.79 ± 0.09         | 2.19 ± 0.09         |
| AS 205B <sup>a</sup> ..... | 1.31                   | 213           | 1.10 ± 0.21         | 0.94 ± 0.10         | 0.91 ± 0.12         |

<sup>a</sup> AS 205B is a spectroscopic binary. See the Appendix for details.

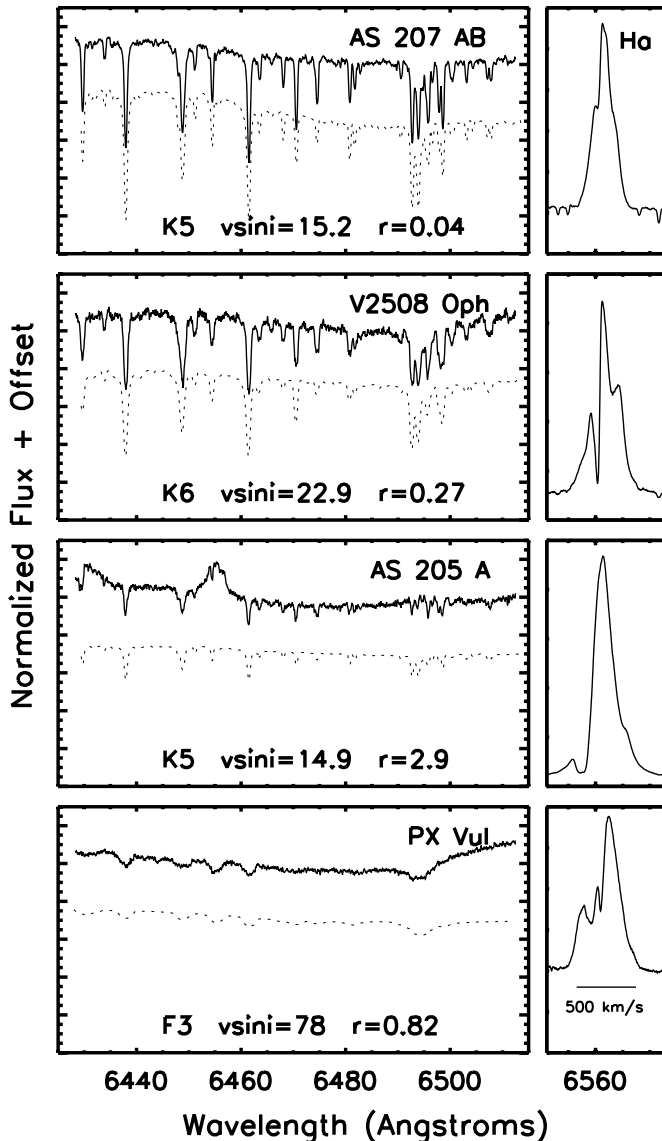


FIG. 1.—Portions of the Keck/HIRES spectra within the  $R$  band (left) and  $H\alpha$  emission profiles (right); both panels have the same wavelength scale. The best-fit dwarf standards, rotationally broadened and optically veiled, are shown as dashed lines for comparison. The strong, broad  $H\alpha$  emission profiles suggest that all stars are accreting.

truncation radii (§ 3.1.3). Inferred  $v \sin i$  values allow estimates of disk corotation radii (§ 3.1.4) for comparison purposes.

### 3.1. Stellar and Accretion Properties

#### 3.1.1. Stellar Properties

We determined radial velocities, rotational velocities, spectral types, and continuum excesses for our sample from optical spectra (Table 1), following White & Hillenbrand (2004). Radial velocities and  $v \sin i$  values are estimated by fitting a parabola to the peak of the cross-correlation functions, derived using dwarf stars of similar spectral type. The spectral types and the optical veiling levels at  $\sim 6500$  and  $\sim 8400$  Å (defined as  $r_{R,I} = F_{\text{excess}}/F_{\text{photosphere}}$ ) are established simultaneously by comparisons with artificially veiled dwarf standards.<sup>3</sup> For the binary

<sup>3</sup> The lines used to measure spectral types and veilings are not gravity dependent, and thus dwarf standards are suitable even though they have higher surface gravities than our T Tauri sample (see White & Hillenbrand 2004 for further discussion).

AS 205, spectral types are determined for both components from spatially resolved spectra. In this discussion, we focus on AS 205A, but analysis of AS 205B, itself resolved into a spectroscopic binary, is included in the Appendix. The binary AS 207 is spatially unresolved in the spectral data, preventing extraction of individual components. However, the large flux ratio for the AS 207 components (Table 3) suggests that the spectral type of the system is dominated by that of AS 207A. AS 207A, V2508 Oph, and AS 205A have mid-K spectral types, while PX Vul is hotter, with a spectral type of F3.

Since the optical photometry does not resolve the components of AS 205 and AS 207 (§ 2.4), we measure flux ratios from AO or spectroscopic observations and use the spectral types for the components to determine flux ratios at wavelengths where the pairs are spatially unresolved. For AS 205, the two Gaussian fits to echelle spectra (§ 2.4) provide a direct measure of the flux ratios at  $R$  and  $I$  bands of 0.16 and 0.24, respectively. The independently determined spectral types then provide estimates of flux ratios for the spatially unresolved  $UBV$  measurements. For AS 207, the two components are unresolved in the echelle spectra, and we employ a less direct procedure. We assume that the spatially resolved  $J$ -band measurement (§ 2.3) probes the photosphere of each component and then predict flux ratios at the shorter, spatially unresolved wavelengths using the measured spectral type for AS 207A (K5) and an assumed spectral type of M3 for the secondary. The companion's spectral type is consistent with both the observed  $J$ -band flux ratio and the cooler spectral types assigned from near-infrared spectroscopy and photometry for the composite system (Doppmann et al. 2003; Geoffroy & Monin 2001).

Stellar temperatures are assigned based on measured spectral types assuming a dwarf temperature/spectral type relation (e.g., Hillenbrand & White 2004). Extinctions and stellar luminosities are determined by comparing the veiling-corrected  $R - I$  fluxes to those expected from Kurucz models most similar in temperature, assuming  $\log g = 4$  (appropriate for pre-main-sequence stars aged 1–10 Myr; e.g., Piorno Schiavon et al. 1995), the extinction relation of Steenman & Thé (1991), and the distances listed in Table 1. Stellar radii are estimated from the luminosities and temperatures using the Stefan-Boltzmann equation. Temperatures, luminosities, radii, and extinctions for these stars are listed in Table 4. We estimate that the assumed stellar temperatures are accurate to  $\pm 100$  K, while luminosities, radii, and extinction estimates are uncertain by  $\sim 20\%$ – $30\%$ .

Stellar masses and ages are estimated by comparing the luminosities and temperatures with the predictions of pre-main-sequence evolutionary models (Siess et al. 2000).<sup>4</sup> These comparisons lead to masses near  $1 M_{\odot}$  for the 3 K-type stars and  $2 M_{\odot}$  for the F3 star. Stellar ages range from 0.6 to 6.9 Myr (Table 4). While considerable uncertainties in pre-main-sequence evolutionary models may lead to large errors in absolute ages, the relative ages are more secure. Including adopted uncertainties of 100 K for stellar temperature and 30% for stellar luminosity, AS 207A and V2508 Oph appear to be the youngest stars in the sample, while AS 205A is somewhat older, and PX Vul is older still. We note that the apparent spread in ages may also correspond to different accretion histories for different sources, which could lead to variations in the birth line for pre-main-sequence models; thus, the relative ages should be treated with some caution.

<sup>4</sup> We prefer evolutionary models of Siess et al. (2000) because they span a larger range of stellar masses than those of Baraffe et al. (1998), and they are more consistent with measured dynamical masses than the D'Antona & Mazzitelli (1997) models.

### 3.1.2. Mass Accretion Rates

Relative accretion rates for our sample are constrained qualitatively by H $\alpha$  emission lines in our spectra (Fig. 1). Equivalent widths (EWs) of H $\alpha$  and full-widths at 10% of the peak are listed in Table 1. These strong, broad profiles suggest ongoing accretion in all sources (e.g., White & Basri 2003), with relatively smaller accretion rates for AS 207A and V2508 Oph.

Quantitative estimates of mass accretion rates are calculated from the accretion luminosity generated by infalling material (Gullbring et al. 1998),

$$\dot{M} = \frac{L_{\text{acc}} R_*}{GM_* (1 - R_*/R_{\text{in}})}. \quad (1)$$

Here,  $L_{\text{acc}}$  is the accretion luminosity,  $R_*$  is the stellar radius,  $M_*$  is the stellar mass, and  $R_{\text{in}}$  is the inner disk radius. We adopt values of  $R_{\text{in}}$  from Table 5 (using puffed-up inner disk sizes determined from combined  $V^2$  + SED analysis; see § 3.3); these are inner radii of the dust disks and may be somewhat larger than the inner gas radii relevant for this formula (as discussed in § 5.2), which would consequently lead to larger inferred mass accretion rates.

The accretion luminosity,  $L_{\text{acc}}$ , is estimated by applying a bolometric correction factor to a flux excess measured over a limited wavelength range. We calculate accretion luminosities using two methods, one based on measured veiling at  $R$  band (e.g., Hartigan & Kenyon 2003; White & Hillenbrand 2004), and the other based on measured  $U$ -band excess emission (Gullbring et al. 1998). For the first method,  $R$ -band excess luminosities are calculated from the measured veilings and then converted into accretion luminosities using a bolometric correction of 35. The bolometric correction factor is highly uncertain and probably introduces uncertainties of a factor of  $\sim 3$  in the computed accretion luminosities. We also calculate the accretion luminosity from the observed  $U$ -band excess luminosity ( $L_U$ ) following Gullbring et al. (1998),

$$\log(L_{\text{acc}}/L_{\odot}) = 1.09_{-0.18}^{+0.04} \log(L_U/L_{\odot}) + 0.98_{-0.07}^{+0.02}. \quad (2)$$

Although the accretion luminosities calculated using equation (2) use a smaller bolometric correction than for the first method (because of the assumed high temperature of the accretion excess; Calvet & Gullbring 1998), the large photometric uncertainties for our  $U$ -band data (Table 2) introduce errors of a factor of  $\sim 2$ . We find that accretion estimates based on  $U$ -band fluxes are typically higher than those computed from  $R$ -band measurements, although the two estimates are consistent to within a factor of 2. Since the accretion luminosities estimated from both methods have large error bars, we adopt the mean of the two values in our analysis. Inferred accretion luminosities for our sample range from 0.4 to 25.0  $L_{\odot}$  and are listed in Table 4.

Using these adopted values for  $L_{\text{acc}}$ , we calculate mass accretion rates from equation (1). For our sample,  $\dot{M}$  is between  $3.2 \times 10^{-8}$  and  $1.3 \times 10^{-6} M_{\odot} \text{ yr}^{-1}$  (Table 4). The large uncertainties for  $L_{\text{acc}}$  lead to accretion rates that are probably uncertain by a factor of 2–3.

### 3.1.3. Magnetospheric Radii

The expected radius of magnetospheric truncation,  $R_{\text{mag}}$ , is determined by the balance of forces between infalling (accret-ing) material and the stellar dipole field (Königl 1991),

$$\frac{R_{\text{mag}}}{R_*} = 2.27 \left[ \frac{(B_0/1 \text{ kG})^4 (R_*/R_{\odot})^5}{(M_*/M_{\odot})(\dot{M}/10^{-7} M_{\odot} \text{ yr}^{-1})^2} \right]^{1/7}. \quad (3)$$

With the stellar parameters determined in § 3.1.1, the accretion rates calculated in § 3.1.2, and assuming a typical magnetic field strength for T Tauri stars of 2 kG (Johns-Krull et al. 2003), we calculate  $R_{\text{mag}}$  for our sample. Our values for  $R_{\text{mag}}$  range from 0.03 to 0.13 AU (Table 4). Propagating the assumed uncertainties for  $R_*$ ,  $M_*$ , and  $\dot{M}$ , and adopting an uncertainty of 30% for  $B_0$ , we estimate that the magnetospheric radii are uncertain by  $\sim 30\%$ .

### 3.1.4. Corotation Radii

The corotation radius is the radius at which the Keplerian orbital period in the disk equals the stellar rotation period. We derive corotation radii for stars with  $v \sin i$  measurements (Table 1) according to

$$R_{\text{corot}} = (GM_*)^{1/3} \left( \frac{R_*}{v} \right)^{2/3} \leq (GM_*)^{1/3} \left( \frac{R_*}{v \sin i} \right)^{2/3}. \quad (4)$$

Here,  $M_*$  is the stellar mass,  $R_*$  is the stellar radius,  $v \sin i$  is the projected rotational velocity of the star, and  $i$  is the inclination of the system. For AS 207A, where there is a reported photometric period,  $\tau = 6.53$  days (Shevchenko & Herbst 1998; Bouvier 1990), the inclination (and hence the corotation radius) can be determined explicitly. For the remaining sources, without known rotation periods (Shevchenko & Herbst 1998), we derive upper limits. Corotation radii and upper limits range from 0.03 to 0.09 AU and are listed in Table 4. Propagating the uncertainties in  $M_*$ ,  $R_*$ , and  $v \sin i$  (assuming stellar mass and radius are uncertain by  $\sim 30\%$ ), we estimate that the derived corotation radii are uncertain by approximately 20%.

## 3.2. Near-IR Stellar and Excess Fluxes

The measured 2.2  $\mu\text{m}$  visibilities and near-IR SEDs contain information about inner circumstellar disks as well as the central stars, and distinguishing the stellar and excess fluxes is crucial to accurate modeling of the disks. Because the stellar SED peaks closer to 2.2  $\mu\text{m}$  for our current sample than for the hotter stars analyzed in Eisner et al. (2004), this step is especially critical here. In this section we discuss our procedure for removing the stellar component from the  $V^2$  and SED data, and in § 3.3 we model the circumstellar component and determine disk parameters.

The measured SED at near-IR wavelengths is simply the sum of the stellar and disk fluxes. Our 2.2  $\mu\text{m}$  visibilities are given by

$$V_{\text{meas}}^2 = \left( \frac{F_* V_* + F_D V_D}{F_* + F_D} \right)^2 \approx \left( \frac{F_* + F_D V_D}{F_* + F_D} \right)^2, \quad (5)$$

where  $F_*$  is the stellar flux,  $V_* \approx 1$  are the visibilities due to the unresolved central star,  $F_D$  is the circumstellar disk flux, and  $V_D$  are the visibilities due to the disk. A knowledge of the stellar flux at near-IR wavelengths is critical for modeling the circumstellar components of both the 2.2  $\mu\text{m}$  visibilities and the near-IR SEDs. This flux can be estimated using the stellar parameters from § 3.1.1 and extrapolating the veiling-corrected flux measured at optical wavelengths using a Kurucz model. The excess 2.2  $\mu\text{m}$  flux due to the compact circumstellar disk is the difference between the dereddened observed flux and the Kurucz model. These 2.2  $\mu\text{m}$  stellar and excess fluxes are listed in Table 4.

The inferred stellar and excess fluxes are somewhat uncertain, leading to uncertainties in the derived disk parameters. For AS 205A and PX Vul, where the excess flux dominates the

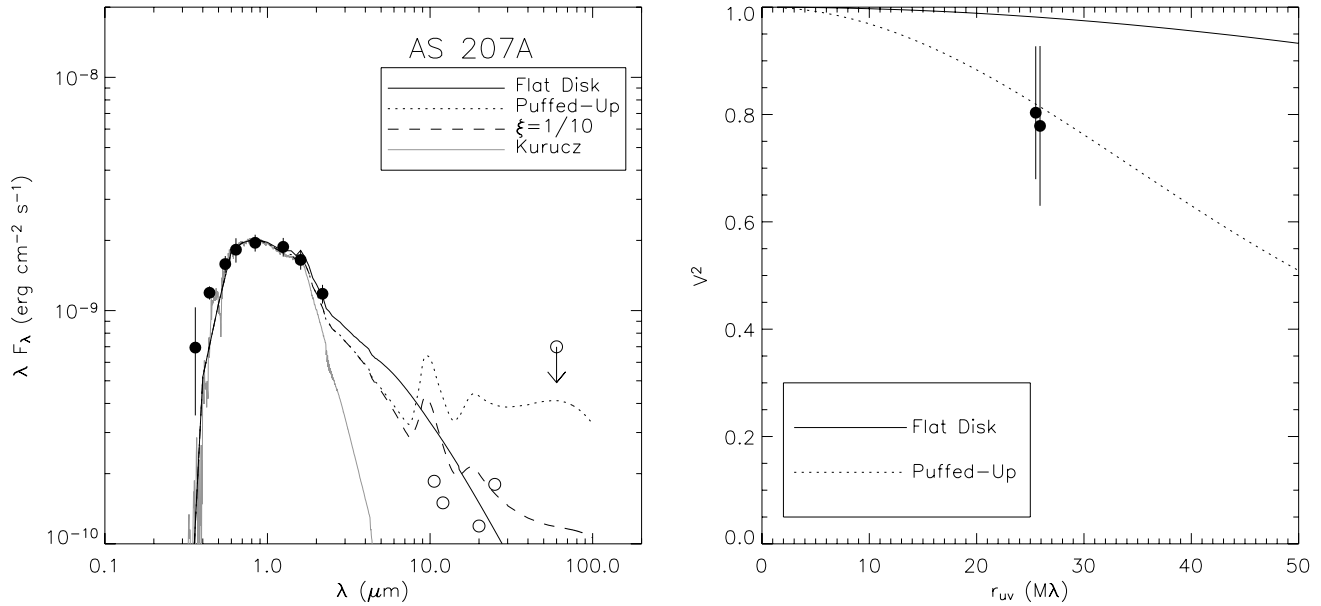


FIG. 2.—*Left*: Reddening-corrected fluxes for AS 207A from optical through near-IR wavelengths (*filled circles*), supplemented with longer wavelength fluxes from the literature (*open circles*; Weaver & Jones 1992; Jensen & Mathieu 1997; Prato et al. 2003; Koresko 2002). Predicted SEDs for geometrically flat accretion disks (*solid line*), and flared disks with puffed-up inner rims (*dotted line*), as well as the Kurucz model atmosphere with the stellar parameters determined in § 3.1.1 (*solid gray line*), are also plotted. Only *RJHK* photometry, probing the star and inner disk, was used in the fits. We also plot the SED predicted by a flared disk model with an intermediate flaring index  $\xi = 1/10$  (*dashed line*). *Right*: Squared visibilities measured with KI, as a function of  $uv$  radius, along with the predictions of different models. The two curves are labeled as in the left panel: the solid line indicates the model determined by fitting a flat accretion disk to the  $V^2 + \text{SED}$  data set, and the dotted line represents the  $V^2$  for the best-fit puffed-up inner disk wall model. For AS 207A, the puffed-up inner disk model provides a superior fit to the data. The long-wavelength photometry is compatible with an unflared outer disk.

emission, uncertainties in the relative fluxes will have little effect on disk parameters. However, when the stellar and excess fluxes are comparable, as for AS 207A and V2508 Oph, there can be significant errors in the fitted disk sizes. For example, 30% errors in  $2.2 \mu\text{m}$  stellar flux lead to size errors of 25% and 23% for AS 207A and V2508 Oph, but only 2% and 7% for AS 205A and PX Vul.

In addition to the central star and circumstellar disk, there may be other contributions to the visibilities and SEDs. Emission on scales between the  $\sim 5$  mas KI fringe spacing and the  $\sim 50$  mas field of view, for example, because of thermal or scattered emission from residual envelopes, will be resolved out and will lower the overall measured visibilities and lead to larger inferred sizes. If the extended emission has a similar spectrum to the star, as expected for scattering from large dust grains, then it will not affect the SED. Extended emission is difficult to constrain, since observations that can resolve faint emission on angular scales smaller than 50 mas are virtually nonexistent. However, previous analysis of the visibilities and SEDs of more luminous Herbig Ae/Be stars indicates small ( $\lesssim 1\%$ ) contributions from extended emission on  $\lesssim 1''$  scales (Eisner et al. 2004). For KI, which has a field of view of only 50 mas, we expect the contribution from extended emission for our less luminous T Tauri star sample to be even smaller.

Near-IR emission may also arise from hot gas in accretion shocks at the stellar photosphere (e.g., Calvet & Gullbring 1998; Gullbring et al. 2000) or from hot optically thin gas in the inner disk (interior to the dust truncation radius; e.g., Akeson et al. 2005). Since these hot gas components are compact compared to emission from the circumstellar dust disk, they would tend to raise the visibilities compared to those predicted by our equation (5), i.e., lead to smaller inferred disk sizes. In contrast, for the measured SEDs hot gas would contribute extra emission, leading to *larger* inferred disk sizes. We expect that the fraction

of near-IR emission from an 8000 K accretion shock (Calvet & Gullbring 1998) will be relatively small compared to peak emission from a 1000–2000 K disk. However, emission from hot gas may cause a measurable effect on the  $2.2 \mu\text{m}$  visibilities and near-IR SEDs for sources with extremely high accretion rates (see § 4.3).

In the analysis below, we assume that near-IR emission from extended dust or hot gas is insignificant compared to the stellar and disk emission. Thus, we model the SED using a Kurucz stellar atmosphere plus thermal emission from a disk and use equation (5) to model the measured visibilities.

### 3.3. Modeling Inner Disk Structure

Equipped with the stellar and circumstellar contributions to the visibilities and SEDs (§ 3.2), we fit the circumstellar components using the two simple disk models described in detail by Eisner et al. (2003, 2004): (1) a geometrically flat accretion disk with a temperature profile  $T(R) \propto R^{-3/4}$  (Lynden-Bell & Pringle 1974), truncated at an inner radius  $R_{\text{in}}$ ; and (2) a flared, irradiated, two-layer disk (Chiang & Goldreich 1997) incorporating a puffed-up inner disk wall at  $R_{\text{in}}$  (Dullemond et al. 2001). The main difference between the two models is the angle of incidence of stellar radiation: for the flat disk, stellar radiation is incident at glancing angles, while the puffed-up inner disk and flared outer surface intercept starlight at more normal angles, leading to additional disk heating. For the second model, the near-IR emission is dominated by the puffed-up inner rim, and the emission appears essentially ringlike at the  $2.2 \mu\text{m}$  wavelength of our interferometric observations. While the geometrically thin disk model assumes blackbody emission, we assume that the opacity for the puffed-up inner disk model is due to astronomical silicate dust (Draine & Lee 1984).

For each model, the parameters relevant for the inner disk structure are the inner radius,  $R_{\text{in}}$ , and the temperature of the

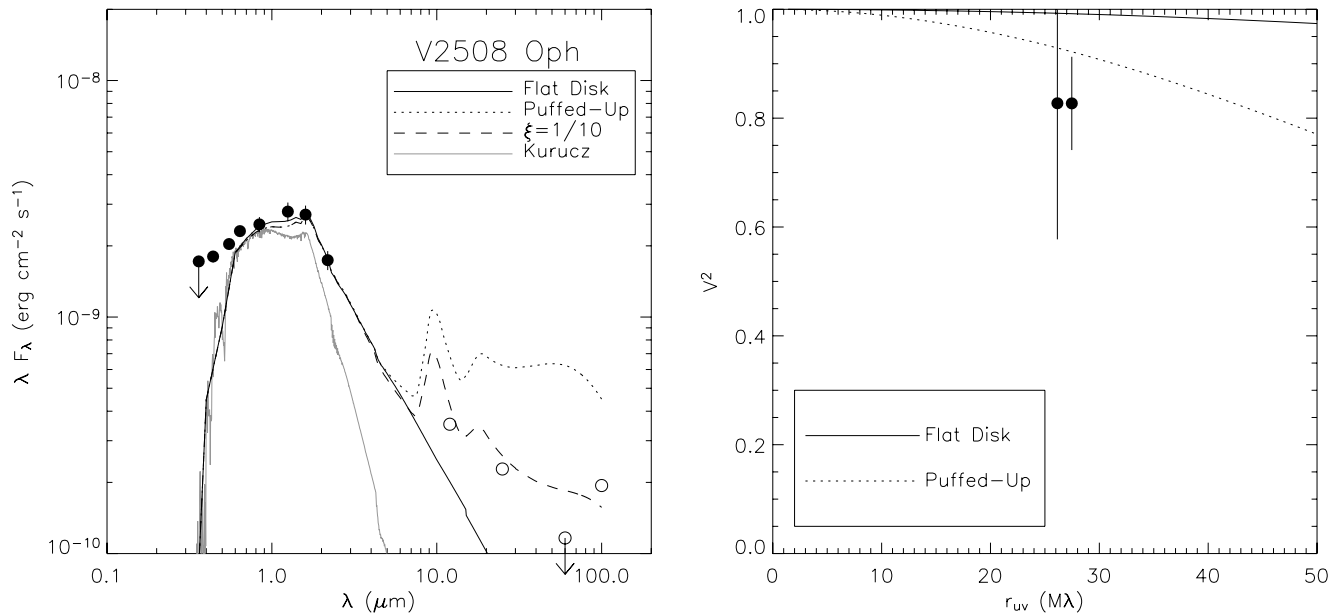


FIG. 3.—SEDs and squared visibilities for V2508 Oph, labeled as in Fig. 2. For this source, the puffed-up inner disk model provides a superior fit to the SED and  $V^2$  data. The *IRAS* photometry for this source is more consistent with a moderately flared disk model (with  $\xi \sim 1/10$ ) than with a flat disk model.

disk at the inner radius,  $T_{\text{in}}$ . Temperatures at other disk radii are specified by these parameters and the assumed temperature profiles for the disk models. The  $V^2$  and SED data (and associated error bars) used in the modeling are shown in Figures 2–5. We use only *RJHK* photometry, and deconvolve the *RI* fluxes, so that the data traces only the inner disk, uncontaminated by hot accretion excess emission, which can dominate at shorter wavelengths.

With the limited amount of data available (2–4 visibilities, and five photometric points for each source), we consider only face-on disk models here. As discussed in Eisner et al. (2004), including inclination in the models may affect the results. Unless the baseline position angle corresponds with the major axis of an inclined disk, the size inferred from  $V^2$  measurements for a

face-on model would be underestimated with respect to the inferred size for an inclined model. Similarly, the face-on assumption would lead to an underestimate of disk size from SED data, since a face-on disk produces more near-IR flux than an inclined disk of the same size. Further interferometric observations, probing a range of position angles, are necessary to constrain the parameters of inclined disk models. However, assuming that our sources are not close to edge-on (which is reasonable given that the central stars are unobscured), inclination effects will not substantially alter the results presented here for face-on disk models.

We fit our  $2.2 \mu\text{m}$  KI visibilities and SED data simultaneously and determine the best-fit parameter values,  $R_{\text{in}}$  and  $T_{\text{in}}$ ,

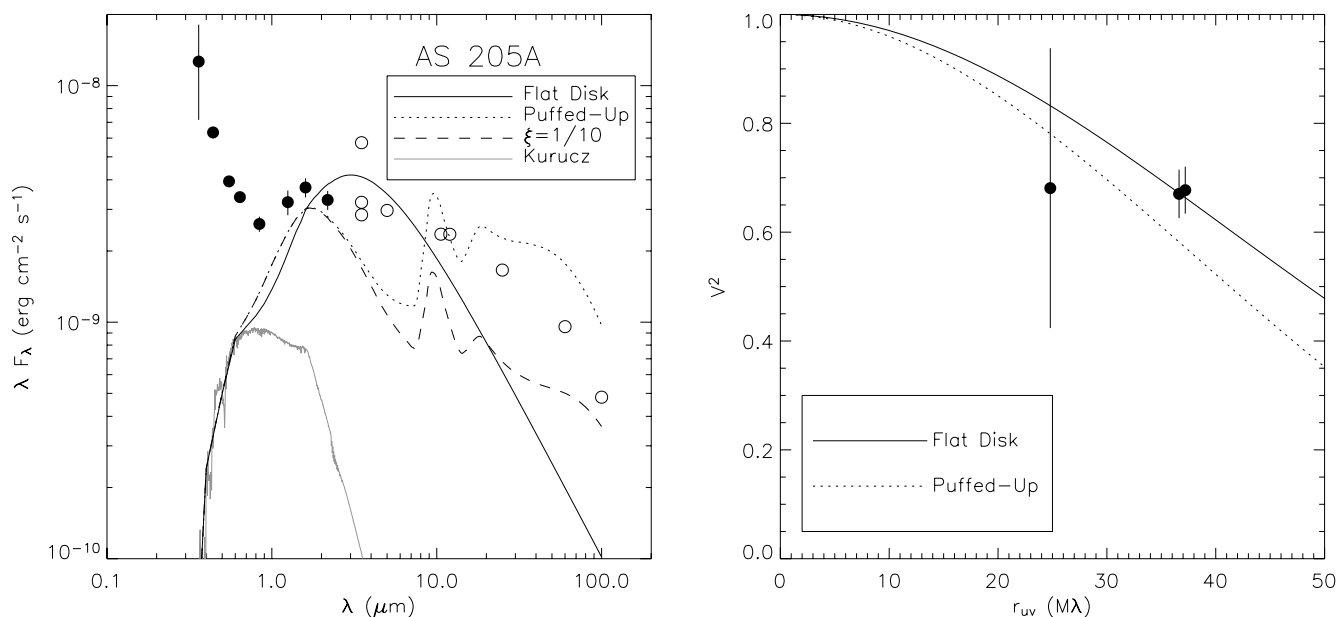


FIG. 4.—SEDs and squared visibilities for AS 205A, labeled as in Fig. 2. For this source, the flat disk model provides a better fit than the puffed up inner disk model to the SED and  $V^2$  data, although neither model fits very well. These poor fits are likely due to near-IR emission from hot accretion shocks that is not accounted for in our models. The fact that the long-wavelength photometry lies above the model predictions suggests that flaring and accretion heating are important in the outer disk.

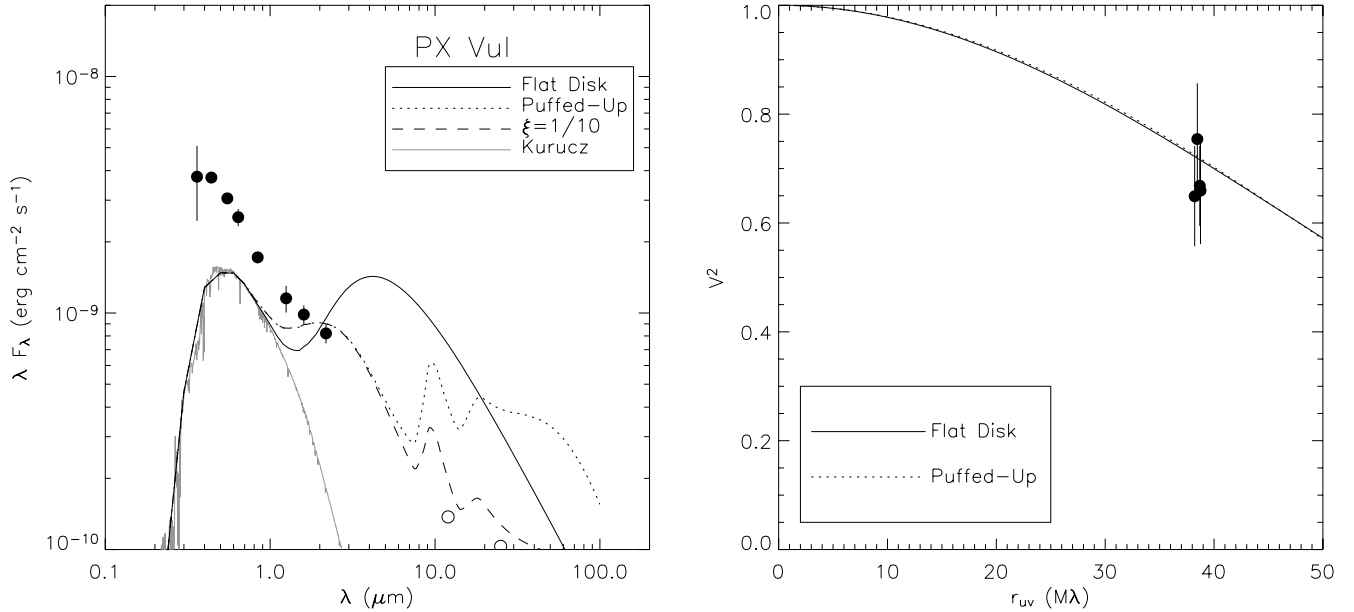


FIG. 5.—SEDs and squared visibilities for PX Vul, labeled as in Fig. 2. For this source, the puffed-up inner disk model provides a superior fit to the SED and  $V^2$  data. The long-wavelength photometry is compatible with an unflared outer disk. Note that for this object, both models fit the  $V^2$  data, but lead to significant deviations in the near-IR SEDs, while for other sources, the SEDs are similar but the  $V^2$  predictions differ (Figs. 2–4); this is due to the fact that we have more  $V^2$  measurements for PX Vul, and the combined  $V^2 + \text{SED}$  fits are therefore dominated by the interferometric rather than the photometric data.

by calculating  $\chi^2$  for models over a grid of inner radii and temperatures. In practice, we fit for the directly observable angular (rather than linear) size of the inner radius  $\theta_{\text{in}}$ ; best-fit values are converted to linear sizes using the distances in Table 1. We consider  $\theta_{\text{in}}$  ranging from 0.1 to 10 mas in increments of 0.01 mas (spanning the approximate angular resolution of KI) and  $T_{\text{in}}$  ranging from 1000 to 2500 K in 100 K increments (bracketing values expected for dust sublimation; e.g., Salpeter 1977; Pollack et al. 1994). For each model, we calculate the  $\chi^2$  of the combined  $V^2 + \text{SED}$  data set, where each data point is weighted by its measurement uncertainty, and we find the inner disk size and temperature for which  $\chi^2$  is minimized;  $1 \sigma$  uncertainties on the best-fit parameters are determined in the standard way (e.g., Eisner et al. 2004). Best-fit parameters,  $1 \sigma$  uncertainties, and reduced  $\chi^2$  values are listed in Table 5. Puffed-up inner disk models generally provide small  $\chi^2$  values (indicating good fits to the data), with inner disk sizes and temperatures ranging from 0.12 to 0.32 AU and from 1000 to 1800 K, respectively. In contrast, flat disk models fit the data poorly and suggest smaller inner disk sizes (0.02–0.22 AU) and higher temperatures (1400–2400 K).

The poor fits of flat disk models to the data are consistent with previous observations, which showed that sizes determined from

near-IR interferometry are often larger than those determined from SED modeling (e.g., Akeson et al. 2000; Millan-Gabet et al. 2001; Eisner et al. 2003). We investigate this issue here by fitting the visibility and SED data separately. For the SEDs, we use the same procedure and parameter grid as for the combined analysis. For the visibilities, where we have fewer data points, we fit only for  $\theta_{\text{in}}$ , assuming the value of  $T_{\text{in}}$  determined from the combined analysis. The best-fit parameter values, uncertainties, and reduced  $\chi^2$  values are included in Table 5. We note that for the small numbers of visibility measurements, the reduced  $\chi^2$  are often very small, indicating poor constraints on the models. The results indicate that the  $V^2$  or SED data individually can be fitted reasonably well with either model, although the puffed-up inner disk model provides somewhat lower  $\chi^2$  values for the SED fits. For most sources, the inner size for flat disk models inferred from the visibilities is  $\geq 5$  times larger than inferred from the SEDs. The puffed-up inner disk models, in contrast, find best-fit sizes from the  $V^2$  or SEDs generally consistent within the  $1 \sigma$  uncertainties (Table 5).

From the SEDs alone, we cannot distinguish between flat and puffed-up inner disk models, but combined  $V^2 + \text{SED}$  analysis shows that puffed-up inner disk models are preferred (Table 5).

TABLE 4  
INFERRED STELLAR AND ACCRETION PROPERTIES

| Source          | $T_*$<br>(K) | $L_*$<br>( $L_\odot$ ) | $R_*$<br>( $R_\odot$ ) | $A_V$<br>(mag) | $M_*$<br>( $M_\odot$ ) | $\tau_*$<br>(Myr) | $L_{\text{acc}}$<br>( $L_\odot$ ) | $\dot{M}$<br>( $M_\odot \text{ yr}^{-1}$ ) | $R_{\text{mag}}$<br>(AU) | $R_{\text{corot}}$<br>(AU) | $F_{*,K}$<br>(Jy) | $F_{D,K}$<br>(Jy) |
|-----------------|--------------|------------------------|------------------------|----------------|------------------------|-------------------|-----------------------------------|--|--------------------------|----------------------------|-------------------|-------------------|
| AS 207A .....   | 4400         | 2.7                    | 2.9                    | 1.6            | 1.2                    | 1.1               | 0.4                               | $3.2 \times 10^{-8}$                       | 0.13                     | 0.09                       | 0.59              | 0.27              |
| V2508 Oph ..... | 4200         | 3.3                    | 3.5                    | 3.5            | 0.9                    | 0.6               | 1.6                               | $2.3 \times 10^{-7}$                       | 0.11                     | $\leq 0.07$                | 0.82              | 0.45              |
| AS 205A .....   | 4400         | 1.3                    | 2.0                    | 3.6            | 1.2                    | 3.2               | 13.0                              | $7.2 \times 10^{-7}$                       | 0.03                     | $\leq 0.07$                | 0.27              | 2.12              |
| PX Vul .....    | 6600         | 13.7                   | 2.9                    | 2.0            | 1.9                    | 6.9               | 25.0                              | $1.3 \times 10^{-6}$                       | 0.04                     | $\leq 0.03$                | 0.13              | 0.46              |

NOTES.—Stellar parameters, accretion luminosities and rates, and magnetospheric and corotation radii determined using high-resolution optical spectra and *UBVRI* photometry (§ 3.1). Stellar and disk fluxes at  $2.2 \mu\text{m}$  ( $F_{*,K}$  and  $F_{D,K}$ ) determined using Kurucz models (with measured  $T_*$ ,  $R_*$ , and adopted distances from Table 1) and dereddened observed photometry (§ 3.2). As discussed in § 3.1, we estimate that  $T_*$  is uncertain by  $\pm 100$  K;  $L_*$ ,  $R_*$ ,  $A_V$ ,  $R_{\text{mag}}$ , and  $R_{\text{corot}}$  are uncertain by  $\sim 30\%$ ;  $L_{\text{acc}}$  and  $\dot{M}$  are uncertain by a factor of 2–3; and  $F_{*,K}$  and  $F_{D,K}$  have error bars of  $\sim 30\%$ – $50\%$ . The uncertainties on  $M_*$  and  $\tau_*$  are more difficult to ascertain, since they depend on pre-main-sequence evolutionary models; however, we estimate that the relative uncertainties for these parameters are  $\sim 30\%$ – $50\%$ .

TABLE 5  
DISK PARAMETERS FROM NEAR-IR INTERFEROMETRY AND SEDS

| SOURCE<br>(1)                | FLAT DISKS        |                             |                            | FLARED, PUFFED-UP DISKS |                             |                            |
|------------------------------|-------------------|-----------------------------|----------------------------|-------------------------|-----------------------------|----------------------------|
|                              | $\chi_r^2$<br>(2) | $R_{\text{in}}$ (AU)<br>(3) | $T_{\text{in}}$ (K)<br>(4) | $\chi_r^2$<br>(5)       | $R_{\text{in}}$ (AU)<br>(6) | $T_{\text{in}}$ (K)<br>(7) |
| Combined $V^2$ + SED Results |                   |                             |                            |                         |                             |                            |
| AS 207A .....                | 1.070             | $0.04^{+0.01}_{-0.02}$      | $1500^{+300}_{-100}$       | 0.208                   | $0.23^{+0.11}_{-0.10}$      | $1000^{+200}_{-100}$       |
| V2508 Oph .....              | 1.409             | $0.02^{+0.17}_{-0.01}$      | $2400^{+100}_{-1300}$      | 0.981                   | $0.12^{+0.10}_{-0.10}$      | $1500^{+900}_{-300}$       |
| AS 205A .....                | 3.729             | $0.07^{+0.01}_{-0.01}$      | $1900^{+100}_{-100}$       | 6.072                   | $0.14^{+0.01}_{-0.01}$      | $1900^{+100}_{-100}$       |
| PX Vul .....                 | 3.049             | $0.22^{+0.01}_{-0.03}$      | $1400^{+100}_{-100}$       | 1.072                   | $0.32^{+0.01}_{-0.04}$      | $1500^{+100}_{-100}$       |
| $V^2$ -only Results          |                   |                             |                            |                         |                             |                            |
| AS 207A .....                | 0.010             | $0.17^{+0.04}_{-0.05}$      | 1500                       | 0.010                   | $0.25^{+0.06}_{-0.07}$      | 1000                       |
| V2508 Oph .....              | 0.003             | $0.10^{+0.04}_{-0.03}$      | 2400                       | 0.003                   | $0.20^{+0.04}_{-0.13}$      | 1500                       |
| AS 205A .....                | 0.211             | $0.07^{+0.01}_{-0.01}$      | 1900                       | 0.224                   | $0.13^{+0.01}_{-0.01}$      | 1900                       |
| PX Vul .....                 | 0.234             | $0.23^{+0.01}_{-0.01}$      | 1400                       | 0.234                   | $0.34^{+0.03}_{-0.02}$      | 1500                       |
| SED-only Results             |                   |                             |                            |                         |                             |                            |
| AS 207A .....                | 0.473             | $0.04^{+0.01}_{-0.02}$      | $1500^{+300}_{-100}$       | 0.327                   | $0.23^{+0.11}_{-0.23}$      | $1000^{+300}_{-100}$       |
| V2508 Oph .....              | 0.969             | $0.02^{+0.03}_{-0.01}$      | $2400^{+100}_{-800}$       | 0.870                   | $0.07^{+0.08}_{-0.07}$      | $1900^{+600}_{-500}$       |
| AS 205A .....                | 6.851             | $0.06^{+0.01}_{-0.01}$      | $2000^{+200}_{-100}$       | 4.796                   | $0.23^{+0.01}_{-0.03}$      | $1600^{+100}_{-100}$       |
| PX Vul .....                 | 1.341             | $0.05^{+0.03}_{-0.01}$      | $2400^{+100}_{-400}$       | 0.842                   | $0.21^{+0.06}_{-0.04}$      | $1800^{+200}_{-200}$       |

NOTES.—Cols. (2)–(4): Reduced  $\chi^2$  values, inner radii, and inner temperatures for best-fit flat accretion disk models. Cols. (5)–(7):  $\chi_r^2$ ,  $R_{\text{in}}$ , and  $T_{\text{in}}$  for best-fit puffed-up inner disk models. Results are shown for fits to combined  $V^2$  + SED data sets as well as  $V^2$  and SEDs individually. For the  $V^2$ -only fits, we assumed the best-fit temperature from the combined  $V^2$  + SED analysis, fitting only for  $R_{\text{in}}$ .

Qualitatively, this additional constraint comes from the spatially resolved information contained in the  $V^2$  data. While near-IR SEDs constrain both the temperature and size of the inner disk, these parameters are degenerate with the spatial and temperature profiles, and thus SED fits are not unique; one can find a suitable fit for either the geometrically thin or puffed-up inner disk models by varying  $T_{\text{in}}$  and  $R_{\text{in}}$ . Combining SEDs with even a limited amount of interferometric data, we can measure *directly* the size of the inner disk, thereby breaking the degeneracy inherent in SED-only modeling and enabling us to distinguish between puffed-up and geometrically flat inner disk models.

The measured sizes discussed above are determined directly from the data. Since we separated the circumstellar components of the visibilities and SEDs from the stellar contributions in § 3.2, the measured disk sizes do not depend on stellar properties or disk accretion rates; i.e.,  $R_{\text{in}}$  and  $T_{\text{in}}$  are chosen simply to provide the best fit to the observations. Thus, the inner disk structure for our best-fit models is fully specified by  $R_{\text{in}}$ ,  $T_{\text{in}}$ , and the assumed temperature profiles. Below, we investigate whether the stellar and accretion luminosities in these sources can provide sufficient disk heating to match the measured inner radii and temperatures, providing an additional test of whether the measured sizes are consistent with the physical models.

For flat disk models, the expected temperature in the disk at 1 AU depends on heating by both stellar radiation and viscous dissipation of accretion energy (Lynden-Bell & Pringle 1974),

$$T_{1 \text{ AU}} = \left[ 2.52 \times 10^{-8} \left( \frac{R_*}{R_\odot} \right)^3 T_*^4 + 5.27 \times 10^{10} \left( \frac{M_*}{M_\odot} \right) \left( \frac{\dot{M}}{10^{-5} M_\odot \text{ yr}^{-1}} \right) \right]^{1/4}. \quad (6)$$

Thus, the expected disk temperature depends on  $T_*$ ,  $R_*$ ,  $M_*$ , and  $\dot{M}$ . Using the value of  $T_{1 \text{ AU}}$  computed for our inferred stellar and accretion parameters (§ 3.1), we predict the radius in the disk where  $T = T_{\text{in}}$  (where  $T_{\text{in}}$  is determined from combined  $V^2$  + SED analysis),

$$\frac{R_{\text{flat}}}{\text{AU}} = \left( \frac{T_{1 \text{ AU}}}{T_{\text{in}}} \right)^{4/3}. \quad (7)$$

For the passive disk model with a puffed-up inner wall, the expected radius where  $T = T_{\text{in}}$  depends on the total luminosity incident on the inner disk,

$$R_{\text{puffed-up}} = \sqrt{\frac{L_* + L_{\text{acc}}}{4\pi\sigma T_{\text{in}}^4}} (1 + f). \quad (8)$$

Here,  $f$  is the ratio of the inner disk width to the inner radius, which we have assumed to be 0.10 (Dullemond et al. 2001). Equation (8) includes the effects of accretion luminosity,  $L_{\text{acc}}$ , in addition to the stellar luminosity (Muzerolle et al. 2003).

Expected inner radii for the two models, with and without accretion heating, are listed in Table 6. We compare these predictions with our measured sizes: for the puffed-up inner disk model, we use sizes measured from  $V^2$  + SED data, while for the flat disk model, which provides poor fits to combined data sets, we use the inner disk sizes measured from  $V^2$ -only data. Measured inner disk sizes are roughly consistent with expectations for puffed-up inner disk models based on the stellar parameters determined in § 3.1.1. Moreover, for the high accretion rate source AS 205A, the predicted size is more consistent with the measured size when accretion luminosity is included, demonstrating the importance of accretion in the disk structure for this object. In contrast, for AS 207A, V2508 Oph, and PX Vul, the predicted

TABLE 6  
MEASURED VERSUS PREDICTED INNER DISK SIZES

| SOURCE          | FLAT DISKS                    |                                     |  | FLARED, PUFFED-UP DISKS       |                                     |  |
|-----------------|-------------------------------|-------------------------------------|--|-------------------------------|-------------------------------------|--|
|                 | $R_{\text{in, meas}}$<br>(AU) | $R_{\text{in, } \dot{M}=0}$<br>(AU) | $R_{\text{in, } \dot{M} \neq 0}$<br>(AU) | $R_{\text{in, meas}}$<br>(AU) | $R_{\text{in, } \dot{M}=0}$<br>(AU) | $R_{\text{in, } \dot{M} \neq 0}$<br>(AU) |
| AS 207A .....   | $0.17^{+0.04}_{-0.05}$        | 0.03                                | 0.04                                     | $0.23^{+0.11}_{-0.10}$        | 0.26                                | 0.28                                     |
| V2508 Oph ..... | $0.10^{+0.04}_{-0.03}$        | 0.02                                | 0.03                                     | $0.12^{+0.10}_{-0.10}$        | 0.13                                | 0.16                                     |
| AS 205A .....   | $0.07^{+0.01}_{-0.01}$        | 0.01                                | 0.07                                     | $0.14^{+0.01}_{-0.01}$        | 0.05                                | 0.17                                     |
| PX Vul .....    | $0.23^{+0.01}_{-0.01}$        | 0.06                                | 0.15                                     | $0.32^{+0.01}_{-0.04}$        | 0.27                                | 0.46                                     |

NOTES.—Measured sizes ( $R_{\text{in, meas}}$ ) taken from Table 5, compared to expectations for disk models based on inferred inner disk temperatures and stellar parameters. For the puffed-up inner disk models, we use the sizes measured from combined  $V^2 + \text{SED}$  analysis, while for the flat disk models, where models generally provide poor fits to the  $V^2$  and SED values simultaneously, we use measured sizes from  $V^2$ -only analysis. Expected inner disk sizes for the flat and puffed-up disk models are calculated from eqs. (7)–(8), assuming no accretion ( $R_{\text{in, } \dot{M}=0}$ ) and using the inferred accretion rates from Table 1 ( $R_{\text{in, } \dot{M} \neq 0}$ ).

sizes of puffed-up inner disk models with  $\dot{M} = 0$  are compatible with the measured sizes (Table 6), suggesting that stellar irradiation is the dominant effect in puffing up the inner disk edges. Expected sizes for the flat disk model are smaller than measured values for all sources except AS 205A. These results are compatible with the fact that the puffed-up inner disk models generally fit the visibility and SED data better than the flat disk models.

The best-fit inner disk sizes (Table 5) are larger than both the magnetospheric and corotation radii calculated in § 3.1 (Table 4). We illustrate this graphically in Figure 6, where we plot the  $2.2 \mu\text{m}$  brightness distributions for our best-fit puffed-up inner disk models and indicate the positions of magnetospheric and corotation radii with dotted and dashed lines, respectively. The discrepancy between measured sizes and magnetospheric/corotation radii is relatively small for some sources ( $\lesssim 2$ ) and large for others ( $> 5$ ). The magnitude of these discrepancies depends to some extent on our assumptions. However, more realistic models including inclined disks and potentially lower stellar magnetic fields would actually exacerbate the differences between measured sizes and magnetospheric radii (magnetic fields substantially higher than the assumed 2 kG are unlikely; Johns-Krull et al. 2003).

### 3.4. Large-Scale Disk Structure

In § 3.3 we modeled our *RIJHK* photometry and  $2.2 \mu\text{m}$  visibilities, and determined inner disk radii and temperatures for our sample. These values of  $R_{\text{in}}$ ,  $T_{\text{in}}$  also provide the normalization of the temperature profiles (for our two simple models) in the outer disk regions. Here, we combine our measurements and modeling of the inner disk with longer wavelength photometry (3–100  $\mu\text{m}$ ; Weaver & Jones 1992; Jensen & Mathieu 1997; Prato et al. 2003; Koresko 2002), which probes larger disk radii. Because of source variability and multiple sources within the large *IRAS* beam (as seen in 2MASS images), the uncertainties in this long-wavelength photometry are likely  $\gtrsim 10\%$ . Despite these uncertainties, the long-wavelength fluxes still yield rough constraints on outer disk structure.

We quantify disk flaring by how the height of the disk increases with radius:  $H/R \propto R^\xi$ . For a flat disk,  $\xi = -1$ , while for a fully flared disk in hydrostatic equilibrium,  $\xi = 2/7$  (Chiang & Goldreich 1997). These two extremes correspond to the flat and puffed-up disk models used above. However, dust settling and/or grain growth could result in other values for  $\xi$  (Dullemond & Dominik 2004a, 2004b). Here, we also consider the case of a somewhat, but not fully, flared disk with  $\xi = 1/10$ . Comparison of the unflared, somewhat flared, and fully flared models with the

data give a qualitative measure of the degree of flaring. Inclination effects, which are not included in our face-on models, will also suppress the long-wavelength flux (because of the smaller projected surface area), mimicking the effects of flatter disks. Thus, we do not attempt to determine  $\xi$  exactly, instead maintaining a qualitative approach.

The outer disk geometry, as illustrated by the long-wavelength photometry, seems to vary from source to source (Figs. 2–5). In some sources (AS 207A and PX Vul), flatter outer disks are consistent with the data, while other objects (V2508 Oph and AS 205A) require significant outer disk flaring to explain the data.

## 4. RESULTS FOR INDIVIDUAL SOURCES

Figures 2–5 show the flat (*solid lines*) and puffed-up (*dotted lines*) disk models that provide the best fits to combined  $V^2 + \text{SED}$  data sets. For each source, see Table 5 for best-fit  $R_{\text{in}}$ ,  $T_{\text{in}}$ , and reduced  $\chi^2$  values of these models. In general, puffed-up inner disk models with inner temperatures ranging from 1000 to 1800 K provide good fits to the data, while flat disk models provide poor fits to the SED and  $V^2$  data.

### 4.1. AS 207A

AS 207A shows a weak near-IR excess and a mass accretion rate lower than other sources in our sample. The visibility and SED data are more consistent with the predictions of a cooler, puffed-up, inner disk model than with a flat disk model ( $\chi_r^2 = 0.21$  vs. 1.07; Fig. 2). Best-fit inner disk sizes and temperatures are  $\sim 0.25$  AU and 1000 K for the puffed-up inner disk model. This size is approximately twice as large as the calculated magnetospheric and corotation radii (Fig. 6).

The *IRAS* photometry for AS 207A is compatible with flat outer disk models. Although AS 207A has a binary companion, the steeply increasing flux ratio across *J*, *H*, and *K* (Table 3) suggests that the companion contributes little to the long-wavelength flux.

### 4.2. V2508 Oph

For V2508 Oph, a source with a relatively small accretion rate, the puffed-up disk model provides a better fit to our  $V^2$  and SED data than the flat disk model ( $\chi_r^2 = 0.98$ , compared with 1.41). While the puffed-up inner disk size determined from the visibilities (0.20 AU) is somewhat larger than that determined from the SED (0.07 AU), the discrepancy has  $< 1 \sigma$  significance, and the fit to the combined  $V^2 + \text{SED}$  data set produces a reasonable  $\chi_r^2$  value (Fig. 3; Table 5). Furthermore, the measured inner disk size agrees well with (but is slightly larger

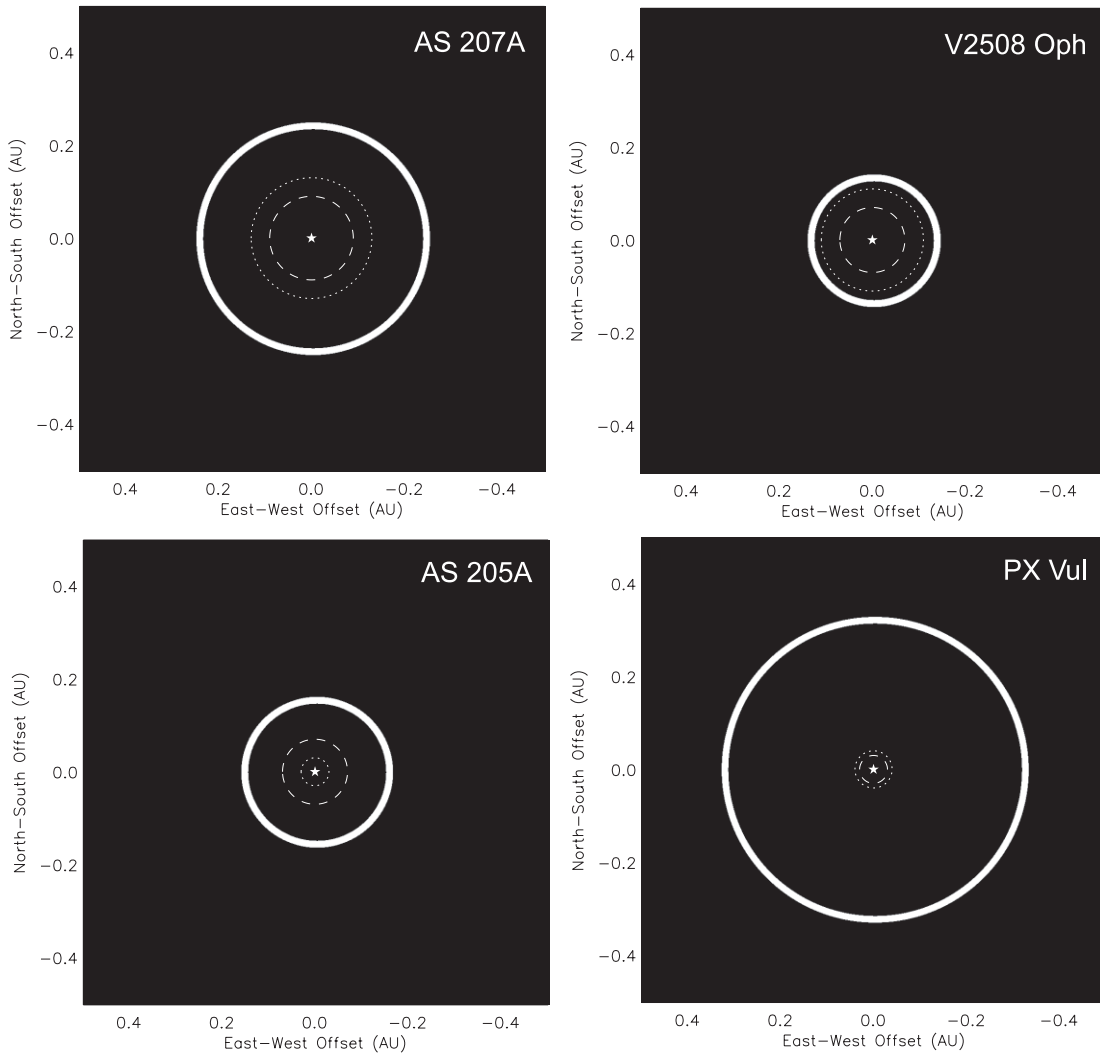


FIG. 6.—Images of the best-fit puffed-up inner disk models for our sample, with inner sizes and temperatures given in Table 5. Because the puffed-up inner rims dominate the  $2.2\ \mu\text{m}$  emission, the images appear ringlike. The magnetospheric truncation radii and (limits on) corotation radii (Table 4) are indicated by dotted and dashed lines, respectively. For AS 205A, V2508 Oph, and PX Vul, the plotted corotation radii are upper limits. The positions of the central stars are indicated with symbols.

than) the magnetospheric truncation radius calculated in § 3.1.3 and the upper limit on corotation radius determined in § 3.1.4 (Fig. 6). The long-wavelength photometry is compatible with an outer disk that is somewhat flared ( $\xi \sim 1/10$ ).

#### 4.3. AS 205A

Fits to the combined  $V^2 + \text{SED}$  data set have  $\chi_r^2 \sim 4\text{--}6$ , mainly because of the poor fit to the SED data. The flat accretion disk model provides a better fit to the combined  $V^2 + \text{SED}$  data set than the puffed-up inner disk model, but both fits are of poor quality, so it is difficult to distinguish between them. The best-fit inner disk sizes range from 0.07 to 0.14 AU, and inner disk temperatures are  $\sim 1900$  K. These fitted inner disk sizes are significantly larger than the magnetospheric truncation radius computed in § 3.1.3 and the upper limit on corotation radius calculated in § 3.1.4 (Fig. 6).

We suggest that the poor fits to the SED data for this source ( $\chi_r^2 \gg 1$ ; Table 5) are due to near-IR emission from an accretion shock, which has not been included in our simple models. As discussed in § 3.2, sources with very high accretion rates may produce substantial near-IR emission from hot accretion shocks; this hot, compact emission would lead to larger inferred sizes

from the SED but smaller inferred sizes from the  $V^2$  measurements. This is consistent with our results for the accretion-dominated source AS 205A ( $L_{\text{acc}}/L_* \sim 10$ ), the only object in our sample for which model fits to the SED predict larger sizes than fits to the visibilities.

Neither the flat disk model nor the flared, puffed-up inner disk model reproduces the far-IR emission well. For the flat disk model, this discrepancy is most likely due to disk flaring, which is ignored in the model. While the flared disk model fits better, the measured  $3\text{--}5\ \mu\text{m}$  fluxes are substantially larger than predicted by the model. Given the extremely high inferred accretion rate for AS 205A, we suggest that viscous dissipation of accretion energy may lead to disk-heating and thus additional puffing that is not included in the model.

#### 4.4. PX Vul

The puffed-up inner disk model provides a good fit to the SED and visibility data for PX Vul ( $\chi_r^2 = 1.09$ ). In contrast, the flat disk model provides a relatively poor fit to the combined data set ( $\chi_r^2 = 3.10$ ; Fig. 5). The best-fit size and temperature for the puffed-up inner disk model are  $\sim 0.32$  AU and 1500 K. Similar to AS 205A, this source has a high mass accretion rate and displays

substantial hot excess emission from an accretion shock. However, the ratio of accretion to stellar luminosity is only  $\sim 2$  for PX Vul, and there seems to be little near-IR emission because of this hot excess; the SED is therefore fitted well by our best-fit disk model. The magnetospheric truncation radius and the corotation radius determined for PX Vul (Table 4) are substantially smaller than the measured inner disk size. Comparison of the *IRAS* photometry with our models suggests that the outer disk may be moderately flared ( $\xi < 1/10$ ).

## 5. DISCUSSION

### 5.1. Emerging Properties of Inner Disks around T Tauri Stars

Inner sizes and temperatures of circumstellar disks around young stars have traditionally been determined by fitting disk models to SEDs (e.g., Beckwith et al. 1990; Hillenbrand et al. 1992; D'Alessio et al. 1999). However, recent interferometric observations of high-mass T Tauri and Herbig Ae/Be stars have shown that inner disks are often much larger than predicted by these SED models (Monnier & Millan-Gabet 2002; Eisner et al. 2004). Our new results, presented in § 4, confirm this trend for lower mass T Tauri stars.

For AS 207A, V2508 Oph, and PX Vul, simple flat accretion disk models suggest much smaller sizes (when fitted to SEDs) than those determined interferometrically. Models incorporating puffed-up inner walls and flared outer disks provide better fits to our  $V^2$  and SED data than the simple flat disk models. This is consistent with previous studies of more massive Herbig Ae stars (Eisner et al. 2004; Leinert et al. 2004) and suggests that truncated disks with puffed-up inner walls describe lower mass T Tauri stars in addition to more massive objects.

The one source in our sample for which the observed  $V^2$  and SED values may be consistent with a simple flat accretion disk model is AS 205A, the object with the highest ratio of accretion to stellar luminosity. Recent observations of another accretion-dominated source, FU Ori, have shown a flat disk model to be appropriate (Malbet et al. 2005). Thus, the vertical structure of the inner disk may depend on the relative magnitude of stellar and accretion luminosities. However, as discussed in § 4.3, a more complicated model that accounts for near-IR emission from accretion shocks is probably necessary to accurately fit the data for AS 205A, and we cannot rule out a puffed-up inner disk with our current analysis.

### 5.2. Dust Sublimation and Magnetospheric Truncation

The truncated disks around T Tauri and Herbig Ae stars may be explained by dust sublimation, which depends on the disk temperature and dust grain properties. An alternative truncation mechanism is magnetospheric disruption of the disk, which is expected to yield a range of inner disk truncation radii and temperatures depending on accretion rates and stellar magnetic fields (e.g., Kenyon et al. 1996). In reality, both mechanisms may be operative in T Tauri disks: optically thick dust disks (which produce most of the observed near-IR emission) may be truncated by dust sublimation, while an optically thin ionized gas component may be truncated closer to the star by the stellar magnetic field.

The calculated magnetospheric radii (§ 3.1.3; Table 4) are smaller than the puffed-up inner dust disk radii measured from the visibilities and SEDs (Table 5) for all sources in our sample, suggesting that magnetospheric truncation is not a viable mechanism for truncating the dust disks in our sample. Stronger magnetic fields are an unlikely way to reconcile these differences, especially for AS 205A and PX Vul, where  $|\mathbf{B}_*| > 20$  kG would be required to bring the magnetospheric truncation radii

into agreement with the measured sizes. Assuming that accreting disk material travels to  $R_{\text{mag}}$  in the midplane before being funneled along magnetic field lines onto the star, the fact that  $R_{\text{in}} > R_{\text{mag}}$  for all sources suggests that the gaseous component of these disks extends farther inward than the dust.

We speculate that dust disks are truncated by sublimation, while gaseous material in the disk midplane extends all the way to  $R_{\text{mag}}$ . The smaller discrepancies between  $R_{\text{in}}$  and  $R_{\text{mag}}$  for sources with lower accretion rates (Fig. 6) are consistent with this scenario: accretional heating pushes the sublimation radius outward (eq. [8]), leading to a larger measured inner dust disk size, while increased pressure from accreting material compresses the magnetospheric radius (eq. [3]). For AS 207A and V2508 Oph, smaller accretion rates lead to magnetospheric truncation closer to the sublimation radii, consistent with the data. In contrast, the high accretion rates in AS 205A and PX Vul may lead to large dust sublimation radii and small magnetospheric radii, which could explain the larger differences between  $R_{\text{in}}$  and  $R_{\text{mag}}$  in these sources.

Under standard models of magnetospheric accretion, it is expected that  $R_{\text{mag}} \lesssim R_{\text{corot}}$ , since outside of corotation, the centrifugal barrier would prevent accretion of material above the disk midplane (Ghosh & Lamb 1979a, 1979b; Kenyon et al. 1996; Shu et al. 1997). Moreover, the slow rotational velocities of T Tauri stars (compared to expectations for the collapse of rotating clouds; e.g., Hartmann & Stauffer 1989) are often explained by magnetic locking of the stellar rotation to the inner disk, which requires  $R_{\text{mag}} \approx R_{\text{corot}}$  (e.g., Königl 1991; Shu et al. 1994). Figure 6 shows that our results are compatible with these models:  $R_{\text{mag}} \approx R_{\text{corot}}$  for our sample. Although for V2508 Oph and AS 207A, the calculated (upper limits) on corotation radii are somewhat smaller than  $R_{\text{mag}}$ , the estimates agree within adopted uncertainties. Thus, our results are consistent with magnetospheric truncation of the gaseous component of circumstellar disks and magnetic locking of the stellar rotation and the inner (gaseous) disk edge.

### 5.3. Implications for Planet Formation

Our results indicate that dust disks around T Tauri stars are truncated within 0.1–0.3 AU of the central stars. Since dust particles provide the building blocks for planetesimals, and ultimately planets, planet formation in these systems is unlikely interior to  $\sim 0.1$  AU. However, our observations indicate that there is dust in the terrestrial planet forming region (i.e.,  $\lesssim 1$  AU). While our best-fit flat inner disk models predict temperatures near 1 AU between 280 and 500 K (eq. [7]), too hot for ice condensation (e.g., Hayashi 1981), the puffed-up inner disk edges indicated by our data may cast a shadow over inner disk regions (e.g., Dullemond et al. 2001), leading to lower temperatures. Thus, the snow line may be located at smaller radii than predicted by flat inner disk models (e.g., Hayashi 1981; Sasselov & Lecar 2000). The location of the snow line has profound implications for the formation of planets, and snow lines at smaller radii may increase the efficiency of Earth-like planet formation (e.g., Raymond et al. 2004).

Inner disk truncation provides a natural mechanism for halting planetary migration (e.g., Lin et al. 1996) and may therefore be linked with the observed period distribution of close-in extrasolar planets. Specifically, one expects migration to cease in a 2:1 resonance with the inner disk radius, corresponding to  $0.63R_{\text{in}}$  (Lin et al. 1996). Kuchner & Lecar (2002) argue that the disk density may drop precipitously within the dust sublimation radius, and that it is therefore the dust truncation radius that is important for halting migration. For the measured inner dust radii of our sources, migrating planets would be halted between 0.08 and 0.20 AU. While some extrasolar planets are found at these radii,

there is a relative dearth of planets between  $\sim 0.06$  and  $0.6$  AU, and most close-in planets are “piled-up” near  $0.03$ – $0.04$  AU (e.g., Udry et al. 2003). Thus, our measured inner dust disk sizes are larger than expected based on the exoplanet period distribution.

This discrepancy suggests that the gaseous components of disks extend farther toward the star than the dust components, and that planetary migration halts in resonances with these gaseous truncation radii as argued by Lin et al. (1996). Gaseous material within the dust disk truncation radius is also consistent with the discrepancy between measured sizes and calculated magnetospheric radii discussed above. Assuming our inferred magnetospheric radii correspond to the inner edges of gaseous disks, we predict resonant orbits between  $0.02$  and  $0.08$  AU from the central star, compatible with the observed pileup location for migrating exoplanets.

An alternate explanation for the apparent discrepancy between resonant orbits predicted by the dust truncation sizes and those actually observed is that the observed exoplanet period distribution is due to migration that occurred in an earlier evolutionary stage, when smaller disk truncation radii led to smaller resonant orbits. Observations of larger samples, spanning a range of inner radii, are necessary to address this issue properly.

## 6. CONCLUSIONS

We have observed three  $1 M_{\odot}$  T Tauri stars and one  $2 M_{\odot}$  T Tauri star with the Keck Interferometer to constrain the structure of the innermost regions of their circumstellar disks. High-resolution near-IR AO images, optical photometry, and optical spectra aided in the analysis of the interferometry data and enabled us to estimate various properties of the systems, including mass accretion rates and corotation radii.

The main result of our analysis is that inner disks around solar-mass T Tauri stars appear similar to those around higher mass T Tauri and Herbig Ae stars. Specifically, the observations for most sources are more consistent with puffed-up inner disk models than with geometrically flat accretion disk models.

We tested the theory of magnetospheric accretion by comparing our measured inner dust disk radii with calculated corotation and magnetospheric truncation radii. All measured sizes are larger than the magnetospheric and corotation radii. Moreover, the difference between measured sizes and inferred magnetospheric/corotation radii seems to increase with accretion

rate: the discrepancy is small for AS 207A and V2508 Oph, but large for AS 205A and PX Vul. We suggest that accretional heating leads to dust sublimation at radii larger than  $R_{\text{mag}}$ . Since higher accretion rates cause larger sublimation radii but smaller magnetospheric radii, this hypothesis can explain our results. Thus, gaseous disks may extend inward to  $R_{\text{mag}}$ , while dust disks are truncated farther out by sublimation.

Comparison of the observed inner disk sizes with the period distribution of extrasolar planets provides support for the hypothesis that gaseous disks extend farther inward than dust disk truncation radii, since our measured inner disk sizes predict 2:1 resonances (which could halt migration) farther from the star than observed for extrasolar planets. In contrast, inferred magnetospheric radii predict resonant orbits that are compatible with the observed semimajor axis distribution of exoplanets.

The near-IR interferometry data presented in this paper were obtained with the Keck Interferometer (KI), which is supported by NASA. We wish to thank the entire KI team for making these observations possible. Observations were carried out at the W. M. Keck Observatory, which is operated as a scientific partnership among California Institute of Technology, the University of California, and NASA. The Observatory was made possible by the generous financial support of the W. M. Keck Foundation. The authors wish to recognize and acknowledge the cultural role and reverence that the summit of Mauna Kea has always had within the indigenous Hawaiian community. We are most fortunate to have the opportunity to conduct observations from this mountain. The authors also acknowledge the robotic P60 team, whose efforts enabled us to collect the optical photometry data presented in this paper. This publication makes use of data products from the Two Micron All Sky Survey, which is a joint project of the University of Massachusetts and the Infrared Processing and Analysis Center, funded by the National Aeronautics and Space Administration and the National Science Foundation. 2MASS science data and information services were provided by the Infrared Science Archive at IPAC. This work has used software from the Michelson Science Center at the California Institute of Technology. J. A. E. acknowledges support from a Michelson Graduate Research Fellowship.

## APPENDIX

### THE SPECTROSCOPIC BINARY AS 205B

The Keck/HIRES spectrum of AS 205B (Fig. 7; § 2.5) showed it to be a double-lined spectroscopic binary, making AS 205 an hierarchical triple. Since the components of AS 205B, labeled Ba and Bb, are of similar brightness, slowly rotating, and reasonably well separated in velocity, their properties can be determined somewhat independently. We use a technique similar to that described in § 3.1.1, but tailored to fit the components of a spectroscopic binary.

Radial velocities, rotational velocities, spectral types, and continuum excesses for the components of AS 205B are determined from the optical spectra. Radial velocities and  $v \sin i$  values are estimated by fitting the two peaks of the cross-correlation function. AS 205Ba and AS 205Bb have radial velocities of  $-0.30 \pm 0.46$  and  $-17.71 \pm 1.11$  km s $^{-1}$ , respectively. Both have projected rotational velocities below our measurement limits ( $v \sin i_{\text{Ba}} \leq 5.9$  km s $^{-1}$ ,  $v \sin i_{\text{Bb}} \leq 10.2$  km s $^{-1}$ ); the larger limit for AS 205Bb is a consequence of its fainter features. The flux ratio of the components, their spectral types, and the continuum excess of the system [defined here as  $r = F_{\text{excess}}/(F_{\text{Ba}} + F_{\text{Bb}})$ ] are determined simultaneously by comparisons with synthetic spectroscopic binaries, generated by combining dwarf standards at the appropriate velocities. The best fit is determined by minimizing the rms difference between AS 205B and the synthetic binary spectra over several temperature-sensitive regions. The components have spectral types of  $K7 \pm 1$  (AS 205Ba) and  $M0 \pm 1$  (AS 205Bb), and AS 205Ba is slightly brighter ( $[F_{\text{Ba}}/F_{\text{Bb}}]_R = 1.52 \pm 0.12$ ,  $[F_{\text{Ba}}/F_{\text{Bb}}]_I = 1.38 \pm 0.11$ ). The optical veiling of the system ( $r_R = 0.83 \pm 0.12$ ,  $r_I = 0.60 \pm 0.09$ ) suggests ongoing accretion, although it is not possible to determine whether this is onto the primary, the secondary, or both. A high accretion rate is also consistent with the strong and broad H $\alpha$  emission (EW =  $-42.6$  Å; 10% width = 384 km s $^{-1}$ ).

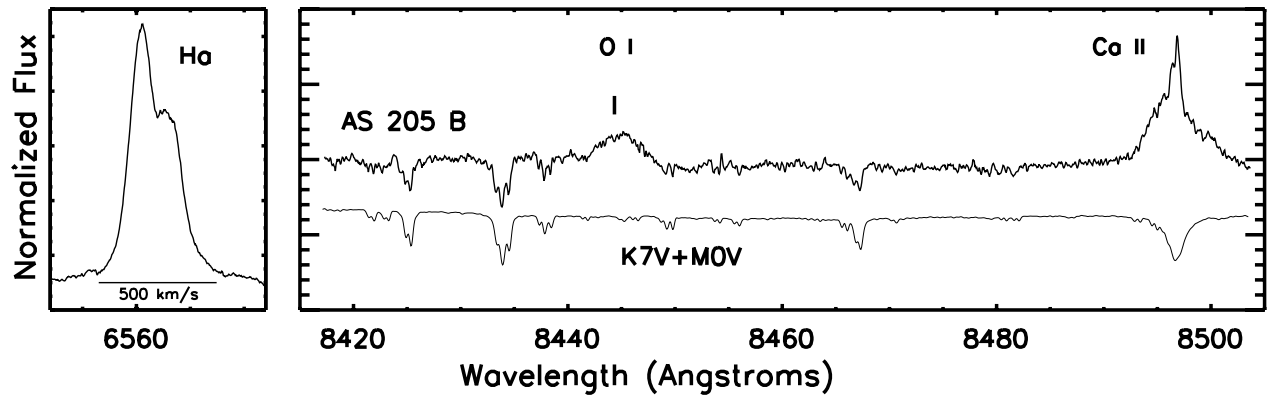


FIG. 7.—Portions of the Keck/HIRES spectrum of the double-lined spectroscopic binary AS 205B at  $H\alpha$  and within the  $I$  band; both panels have the same wavelength scale. The strong, broad  $H\alpha$ ,  $O\ I\ \lambda 8446$ , and  $Ca\ II\ \lambda 8496$  emission features suggest ongoing accretion. The photospheric features are best matched by combining K7 and M0 dwarfs plus an optical excess (see the Appendix).

We estimate the visual extinction and luminosity of each component using the relative fluxes of the spectroscopic binary components at  $R$  and  $I$  in combination with spectral types, veiling, and the total AS 205B fluxes determined in § 3.1.1. We determine visual extinctions of 3.9 and 3.4 mag, and luminosities of 0.44 and 0.26  $L_{\odot}$  for AS 205Ba and AS 205Bb, respectively. Comparison of the effective temperatures (4000 K, 3800 K) and luminosities with the Siess et al. (2000) pre-main-sequence evolutionary models yields stellar masses of 0.74 and 0.54  $M_{\odot}$  and ages of 5.1 and 5.4 Myr for AS 205Ba and AS 205Bb, respectively. Given the uncertainties, all three components of the AS 205 system appear to be coeval.

## REFERENCES

- Adams, F. C., Lada, C. J., & Shu, F. H. 1988, *ApJ*, 326, 865  
Akeson, R. L., Ciardi, D. R., van Belle, G. T., Creech-Eakman, M. J., & Lada, E. A. 2000, *ApJ*, 543, 313  
Akeson, R. L., et al. 2005, *ApJ*, 622, 440  
Baraffe, I., Chabrier, G., Allard, F., & Hauschildt, P. H. 1998, *A&A*, 337, 403  
Barsony, M., Koresko, C., & Matthews, K. 2003, *ApJ*, 591, 1064  
Beckwith, S. V. W., Sargent, A. I., Chini, R. S., & Guesten, R. 1990, *AJ*, 99, 924  
Bertout, C., Basri, G., & Bouvier, J. 1988, *ApJ*, 330, 350  
Boden, A. F., Colavita, M. M., van Belle, G. T., & Shao, M. 1998, *Proc. SPIE*, 3350, 872  
Bouvier, J. 1990, *AJ*, 99, 946  
Calvet, N., & Gullbring, E. 1998, *ApJ*, 509, 802  
Chiang, E. I., & Goldreich, P. 1997, *ApJ*, 490, 368  
Chini, R. 1981, *A&A*, 99, 346  
Colavita, M. M. 1999, *PASP*, 111, 111  
Colavita, M. M., & Wizinowich, P. L. 2003, *Proc. SPIE*, 4838, 79  
Colavita, M. M., et al. 2003, *ApJ*, 592, L83  
D'Alessio, P., Calvet, N., Hartmann, L., Lizano, S., & Cantó, J. 1999, *ApJ*, 527, 893  
D'Antona, F., & Mazzitelli, I. 1997, *Mem. Soc. Astron. Italiana*, 68, 807  
Doppmann, G. W., Jaffe, D. T., & White, R. J. 2003, *AJ*, 126, 3043  
Draine, B. T., & Lee, H. M. 1984, *ApJ*, 285, 89  
Dullemond, C. P., & Dominik, C. 2004a, *A&A*, 417, 159  
———. 2004b, *A&A*, 421, 1075  
Dullemond, C. P., Dominik, C., & Natta, A. 2001, *ApJ*, 560, 957  
Dutrey, A., Guilloteau, S., Duvert, G., Prato, L., Simon, M., Schuster, K., & Menard, F. 1996, *A&A*, 309, 493  
Edwards, S., Hartigan, P., Ghandour, L., & Andriulis, C. 1994, *AJ*, 108, 1056  
Eisner, J. A., Lane, B. F., Akeson, R. L., Hillenbrand, L., & Sargent, A. 2003, *ApJ*, 588, 360  
Eisner, J. A., Lane, B. F., Hillenbrand, L., Akeson, R., & Sargent, A. 2004, *ApJ*, 613, 1049  
Geoffroy, H., & Monin, J.-L. 2001, *A&A*, 369, 239  
Ghez, A. M., Neugebauer, G., & Matthews, K. 1993, *AJ*, 106, 2005  
Ghosh, P., & Lamb, F. K. 1979a, *ApJ*, 232, 259  
———. 1979b, *ApJ*, 234, 296  
Gullbring, E., Calvet, N., Muzerolle, J., & Hartmann, L. 2000, *ApJ*, 544, 927  
Gullbring, E., Hartmann, L., Briceno, C., & Calvet, N. 1998, *ApJ*, 492, 323  
Hartigan, P., & Kenyon, S. J. 2003, *ApJ*, 583, 334  
Hartmann, L., & Stauffer, J. R. 1989, *AJ*, 97, 873  
Hayashi, C. 1981, *Prog. Theor. Phys. Suppl.*, 70, 35  
Hayward, T. L., Brandl, B., Pirger, B., Blacken, C., Gull, G. E., Schoenwald, J., & Houck, J. R. 2001, *PASP*, 113, 105  
Herbig, G. H., & Kameswara Rao, N. 1972, *ApJ*, 174, 401  
Herbst, W., Warner, J. W., Miller, D. P., & Herzog, A. 1982, *AJ*, 87, 98  
Hernández, J., Calvet, N., Briceño, C., Hartmann, L., & Berlind, P. 2004, *AJ*, 127, 1682  
Hillenbrand, L. A., Strom, S. E., Vrba, F. J., & Keene, J. 1992, *ApJ*, 397, 613  
Hillenbrand, L. A., & White, R. J. 2004, *ApJ*, 604, 741  
Jensen, E. L. N., & Mathieu, R. D. 1997, *AJ*, 114, 301  
Johns-Krull, C. M., Valenti, J. A., & Gafford, A. D. 2003, *Rev. Mex. AA Ser. Conf.*, 18, 38  
Kenyon, S. J., Yi, I., & Hartmann, L. 1996, *ApJ*, 462, 439  
Königl, A. 1991, *ApJ*, 370, L39  
Koerner, D. W., & Sargent, A. I. 1995, *AJ*, 109, 2138  
Koresko, C. D. 2002, *AJ*, 124, 1082  
Kuchner, M. J., & Lecar, M. 2002, *ApJ*, 574, L87  
Landolt, A. U. 1992, *AJ*, 104, 340  
Leinert, C., et al. 2004, *A&A*, 423, 537  
Lin, D. N. C., Bodenheimer, P., & Richardson, D. C. 1996, *Nature*, 380, 606  
Lynden-Bell, D., & Pringle, J. E. 1974, *MNRAS*, 168, 603  
Malbet, F., et al. 1998, *ApJ*, 507, L149  
———. 2005, *A&A*, submitted  
Marcy, G. W., & Butler, R. P. 2000, *PASP*, 112, 137  
McCaughrean, M. J., & O'Dell, C. R. 1996, *AJ*, 111, 1977  
Merrill, P. W., & Burwell, C. G. 1950, *ApJ*, 112, 72  
Millan-Gabet, R., Schloerb, F. P., & Traub, W. A. 2001, *ApJ*, 546, 358  
Millan-Gabet, R., Schloerb, F. P., Traub, W. A., Malbet, F., Berger, J. P., & Bregman, J. D. 1999, *ApJ*, 513, L131  
Monnier, J. D., & Millan-Gabet, R. 2002, *ApJ*, 579, 694  
Mora, A., et al. 2001, *A&A*, 378, 116  
Muzerolle, J., Calvet, N., Hartmann, L., & D'Alessio, P. 2003, *ApJ*, 597, L149  
Piorro Schiavon, R., Batalha, C., & Barbuy, B. 1995, *A&A*, 301, 840  
Pollack, J. B., Hollenbach, D., Beckwith, S., Simonelli, D. P., Roush, T., & Fong, W. 1994, *ApJ*, 421, 615  
Prato, L., Greene, T. P., & Simon, M. 2003, *ApJ*, 584, 853  
Raymond, S. N., Quinn, T., & Lunine, J. I. 2004, *Icarus*, 168, 1  
Reipurth, B., & Zinnecker, H. 1993, *A&A*, 278, 81  
Salpeter, E. E. 1977, *ARA&A*, 15, 267  
Sasselov, D. D., & Lecar, M. 2000, *ApJ*, 528, 995  
Shevchenko, V. S., & Herbst, W. 1998, *AJ*, 116, 1419  
Shu, F., Najita, J., Ostriker, E., Wilkin, F., Ruden, S., & Lizano, S. 1994, *ApJ*, 429, 781  
Shu, F. H., Shang, H., Glassgold, A. E., & Lee, T. 1997, *Science*, 277, 1475  
Siess, L., Dufour, E., & Forestini, M. 2000, *A&A*, 358, 593  
Skrutskie, M. F., Meyer, M. R., Whalen, D., & Hamilton, C. 1996, *AJ*, 112, 2168

- Steenman, H., & Thé, P. S. 1991, *Ap&SS*, 184, 9  
Struve, O., & Rudkjøbing, M. 1949, *ApJ*, 109, 92  
Troy, M., et al. 2000, *Proc. SPIE*, 4007, 31  
Udry, S., Mayor, M., & Santos, N. C. 2003, *A&A*, 407, 369  
Vogt, S. S., et al. 1994, *Proc. SPIE*, 2198, 362
- Walker, M. F. 1972, *ApJ*, 175, 89  
Walter, F. M. 1986, *ApJ*, 306, 573  
Weaver, W. B., & Jones, G. 1992, *ApJS*, 78, 239  
White, R. J., & Basri, G. 2003, *ApJ*, 582, 1109  
White, R. J., & Hillenbrand, L. A. 2004, *ApJ*, 616, 998